

STUDY OF RADIOCARBON DETECTION  
BY LASER SPECTROSCOPY

by



DANIEL LABRIÉ, B.Sc.

A Thesis

Submitted to the School of Graduate Studies  
in Partial Fulfilment of the Requirements  
for the Degree  
Master of Science

McMaster University

October 1980

MASTER OF SCIENCE (1980)  
(Physics)

McMASTER UNIVERSITY  
Hamilton, Ontario

TITLE: Study of Radiocarbon Detection by laser spectroscopy

AUTHOR: Daniel Labrie, B.Sc. (Université de Montréal)

SUPERVISOR: Dr. J. Reid

NUMBER OF PAGES: xv, 81

## ABSTRACT

This thesis examines the feasibility of using infrared spectroscopy to carry out radiocarbon dating. Conventional radiocarbon dating techniques are limited in sensitivity by the very small fraction of  $C^{14}$  atoms which disintegrate during the counting period. Our proposed infrared technique does not suffer from this limitation, but we must overcome the problem of interfering infrared spectra caused by stable isotopes, and develop methods for detecting extremely small infrared absorption coefficients.

The apparatus employed consists of a tunable diode laser and a multipass optical cell. Radiocarbon is detected in the form of  $C^{14}O_2$ , and it is shown that interference-free detection can be attained provided the gas sample is cooled to dry ice temperature. To achieve sufficient sensitivity we have developed a second harmonic detection scheme. As part of our optimisation procedure, the experimental and theoretical second harmonic lineshapes were compared over a wide range of experimental conditions. Good agreement was found in all cases.

With the present apparatus, the minimum detectable infrared absorption coefficient was  $\sim 1 \times 10^{-7} \text{ m}^{-1}$ . This compares with a sensitivity of  $\sim 1 \times 10^{-9} \text{ m}^{-1}$  which is required for practical radiocarbon dating. The noise mechanisms which

limit the present sensitivity were investigated in some detail, and results obtained at short time constants in small optical cells are extrapolated to long optical cells and measurement times of several hours. Based on these extrapolations, radiocarbon dating by infrared spectroscopy appears feasible, and will require much smaller carbon samples than is required by conventional disintegration counting techniques.

## ACKNOWLEDGEMENTS

I wish to express my appreciation to my supervisor, Dr. J. Reid, for his guidance and support throughout this work.

I would like to thank Mrs. Helen Kennelly for her typing of the manuscript.

This work was supported, in part, by McMaster University and the Natural Sciences and Engineering Research Council of Canada.

This thesis is dedicated to my parents.

## TABLE OF CONTENTS

		<u>Page</u>
CHAPTER 1	INTRODUCTION	1
CHAPTER 2	EXPERIMENTAL APPARATUS AND DETECTION TECHNIQUES	7
	2.1 Experimental Apparatus	7
	2.2 Second Harmonic Detection	9
CHAPTER 3	MODELLING OF THE SECOND HARMONIC TRANSFER FUNCTION	12
	3.1 Introduction	12
	3.2 Mathematical Model of the Harmonic Detection Technique	13
	3.3 Comparison between Theory and Experiment	16
	3.4 Dependence of the 2f Lineshape upon Gas Pressure	24
	3.5 Conclusions	29
CHAPTER 4	SPECTROSCOPY OF CO <sub>2</sub> NEAR 4.5 μm - DETAILED INVESTIGATION OF THE P-BRANCH OF THE ν <sub>3</sub> BAND OF C <sup>14</sup> O <sub>2</sub>	32
	4.1 Introduction	32
	4.2 Absorption Spectrum of CO <sub>2</sub> near 4.5 μm	32
	4.3 Line-by-Line Evaluation of the P-Branch of C <sup>14</sup> O <sub>2</sub>	37
	4.4 Summary	46

	<u>Page</u>
CHAPTER 5	
ELIMINATION OF INTERFERING BACKGROUND LINES IN CO <sub>2</sub>	47
5.1 Introduction	47
5.2 Measurement of the Lower Level Energy of Interfering Lines	48
5.3 Cooling Effects on the Absorption Spectrum	52
5.4 Summary	57
CHAPTER 6	
NOISE CHARACTERISTICS AND SENSITIVITY LIMITS OF THE LASER ABSORPTION SPECTRO- METER	58
6.1 Introduction	58
6.2 LAS Sensitivity with Short Time Constants	59
6.3 LAS Behaviour at Long Time Con- stants	67
6.4 Conclusions	74
CHAPTER 7	
CONCLUSIONS	77
REFERENCES	79

FIGURE CAPTIONS

		<u>Page</u>
Fig. 2-1	Schematic diagram of the apparatus used for a line-by-line investigation of the $\nu_3$ band of $C^{14}O_2$ . Strong absorption lines were measured using the chopper and direct detection, but second harmonic modulation techniques were employed to measure weak absorption lines [3].	8
Fig. 2-2	$CO_2$ spectrum taken through 200 m path-length at a pressure of 30 Torr. The upper trace shows an absorption spectrum obtained with direct detection. The lower trace was taken with second harmonic detection. Notice the substantial increase in signal-to-noise ratio obtained by switching from direct to second harmonic detection.	10
Fig. 3-1	Qualitative comparison between theory and experiment for the $2f$ lineshape. Note the broadening of the lineshape as the modulation amplitude is varied. As shown in the Figure, the positive part, P, and the negative part, N, of the $2f$ lineshape are defined as the maximum positive and the maximum negative excursion of the $2f$ lineshape from the baseline. The ratio, R, is defined as $R \equiv P/N$ .	17
Fig. 3-2	Plot of the ratio R as a function of the modulation amplitude A for two values of the modulation frequency. Also shown are the theoretical curves fitted to the experiment assuming a linear relationship between the wavelength modulation m and A.	19
Fig. 3-3	Plot of the positive part of the $2f$ lineshape, P as a function of m for both theory and experiment. The maximum value of P is normalized to 1. The experimental A values are fitted to the m values using the scaling factor determined from the ratio measurements.	22



		<u>Page</u>
Fig. 3-4	Scan of the 2f lineshape as a function of wavelength for $m=2.2$ . The experimental curve is taken from the X-Y recorder trace, while the theory is adjusted to fit by using a single scaling factor for each axis.	23
Fig. 3-5	(a) Absorption coefficient as a function of pressure for the vibrational-rotational transition $P(56) 02^0 \rightarrow 02^1$ of $C^{13}O^{16}O_2$ . An absorption line described by a Voigt function is fitted to the experiment with a pressure broadening coefficient of 3.3 MHz/Torr and an integrated intensity of $1.077 \times 10^{-24} \text{ cm}^{-1}/(\text{mol. cm}^{-2})$ . (b) Plot of $P_{\text{max}}$ as a function of pressure. At each pressure, the modulation amplitude was adjusted to maximise the positive part P. The experimental results are scaled to the Voigt function displayed in (a).	26
Fig. 3-6	Calculated P value as a function of m for both pure Doppler and pure Lorentzian broadened lines. The maximum value of each graph is normalised to 1. Also shown are experimental data points obtained with a line which is almost entirely Doppler broadened (the ratio of the Doppler linewidth to the pressure broadened linewidth is 8).	28
Fig. 3-7	Calculated ratio R as a function of m for both lineshapes. Also shown are the measured ratios R for the predominantly Doppler-broadened line. The measured ratios R are obtained from the 2f lineshapes used to produce the results shown in Fig. 3-6. The scaling factor used to relate A to m in Fig. 3-6 is the same as the one employed in this Figure.	30

- Fig. 4-1 Calculated spectrum of  $\text{CO}_2$  in the 4.4  $\mu\text{m}$  region. The  $\nu_3$  fundamental bands of most of the relevant isotopic species are included. The relative strength of each band is normalised to the  $\text{C}^{12}\text{O}^{16}_2$  band-strength on a logarithmic scale, but the individual lines in each band are plotted in a linear fashion. The  $\text{C}^{14}\text{O}_2$   $\nu_3$  band is displayed with an intensity corresponding to a modern carbon sample, ( $\text{C}^{14}/\text{C}^{12} \sim 10^{-12}$ ).
- Fig. 4-2 Detailed  $\text{CO}_2$  spectrum, including hot bands, in the region of the P-branch of  $\text{C}^{14}\text{O}_2$ . All lines are normalised to the strong lines in the fundamental of  $\text{C}^{12}\text{O}^{16}_2$ . Further details are given in the text.
- Fig. 4-3 Results of diode scans over the P(16) and P(14) lines of  $\text{C}^{14}\text{O}_2$ . The lower trace was taken with a pathlength of 200 m through  $\text{CO}_2$  pressure of 30 Torr. For the upper trace the multipass cell was evacuated, and a small cell of  $\text{C}^{14}\text{O}_2$  inserted in the laser beam. Note that the P(16) line is overlapped by line A, while the P(14) line is relatively free from interference. The theoretical absorption spectrum is calculated using the linestrengths of [17]. Line positions indicated by (—) are taken from [10]-[16], while those indicated by (---) are from the less accurate AFGL compilation [17], [18]. Experimental line positions were determined by calibrating the diode tuning rate using a  $\text{N}_2\text{O}$  reference cell [22]-[24].
- Fig. 4-4 Diode scans taken near P(38) line of  $\text{C}^{14}\text{O}_2$  through 200 m pathlength at a pressure of 30 Torr. The upper and lower traces were taken with direct and 2f detection respectively. Two diode traces shown in Fig. 4-4 were recorded with a 10 cm cell of  $\text{C}^{14}\text{O}_2$  placed in the laser beam.

		<u>Page</u>
Fig. 4-5	More sensitive scans of the region around the P(38) $\text{C}^{14}\text{O}_2$ line. The arrow below the lowest trace indicates the position of the P(38) $\text{C}^{14}\text{O}_2$ line. The upper trace is an expanded view of the interfering line which has an intensity equivalent to the intensity of P(38) line with a $\text{C}^{14}\text{O}_2$ concentration of $\sim 1$ ppb.	41
Fig. 4-6	Diode laser scans of the wavenumber region near the P(20) line of $\text{C}^{14}\text{O}_2$ . The upper trace is taken using direct detection. The laser beam passes through a 32 m pathlength of normal $\text{CO}_2$ at 20 Torr, followed by a small cell containing $\text{C}^{14}\text{O}_2$ . For the lower trace the $\text{C}^{14}\text{O}_2$ cell is removed, and second harmonic is employed.	44
Fig. 4-7	More sensitive scans of the region around the P(20) $\text{C}^{14}\text{O}_2$ line. The weak line B is present in normal $\text{CO}_2$ and overlaps the P(20) $\text{C}^{14}\text{O}_2$ line which is represented by the trace at the bottom of the Figure. The displayed P(20) line is equivalent to a $\text{C}^{14}\text{O}_2$ concentration of 1.6 ppb, and the offset from line B is 250 MHz.	45
Fig. 5-1	Schematic diagram of the apparatus used* to determine the lower energy level of the interfering lines.	49
Fig. 5-2	Plot of $\ln(\alpha_H/\alpha_R)$ as a function of lower energy level in $\text{cm}^{-1}$ ( $E_L$ ) for several $\text{CO}_2$ absorption lines. Only those lines which have been unambiguously identified are used in these measurements. Typical error bars are shown, and the straight line through the data points is derived from Equation 5-2, with $T_H = 373$ K. The measured value of $\alpha_H/\alpha_R$ for line B of Fig. 4-7 is also shown.	51
Fig. 5-3	Schematic diagram of the 1 m cold cell.	54

- Fig. 5-4 Plot of  $\ln(\alpha_R/\alpha_C)$  as a function of the lower energy level in  $\text{cm}^{-1}$  ( $E_L$ ) for several  $\text{CO}_2$  absorption lines. Only the lines with known  $E_L$  appearing above the noise level were selected. A straight line is fitted through the data points with  $T_c = 196$  K. 56
- Fig. 6-1 High sensitivity scan of multipass cell set for 40 m. Fringes are caused by interference between the main optical beam making 40 passes through the cell and the much weaker beams, which make 36 (or 44) passes. A second harmonic lineshape corresponding to  $\sim 5$  ppb  $\text{NO}_2$  (or  $10^{-5} \text{ m}^{-1}$  absorption coefficient) is also shown to indicate sensitivity. (Figure taken from Reid et al. [26]). 60
- Fig. 6-2 Effect of additional "jitter" modulation. The LAS is set for second harmonic detection at 6 kHz, but a small jitter modulation at 370 Hz was added to the main 3 kHz sinewave. The upper traces show an expanded view of the fringes as the peak to peak jitter amplitude was varied from 0 to 2 fringe spacings. The lower trace is a repeat of Fig. 6-1, but with jitter amplitude set at 1 fringe spacing. Note the significant improvement in sensitivity as the fringes are electronically "washed out". (Figure taken from Reid et al. [26]) 63
- Fig. 6-3 Lifetime measurement of  $\text{NO}_2$ /air mixtures in a stainless steel multipass cell. The LAS was set to scan repetitively over an  $\text{NO}_2$  doublet at 1604.162, and the cell was filled with air plus a trace of  $\text{NO}_2$  at  $\sim 30$  Torr. The time constant used was only 0.1 s, but the noise level is  $< 1$  ppb. Note the rapid decay of the  $\text{NO}_2$  in the sealed cell. (Figure taken from Reid et al. [26]) 64

Fig. 6-4

The lower trace repeats the measurements of Fig. 6-3, but with the diode laser wavelength held at the centre of the NO<sub>2</sub> absorption line. A mixture of a few ppb NO<sub>2</sub> in air was introduced into the cell, and the concentration monitored with the LAS. The upper trace shows the noise levels which limit sensitivity. Trace A → B is an expanded view of noise under monitoring conditions, taken with a 10 s time constant. Sensitivity is 75 ppt NO<sub>2</sub> or  $1.6 \times 10^{-7} \text{ m}^{-1}$ . At time B, all modulation signals were removed from the laser current, but second harmonic detection at 6 kHz continues. Hence trace B → C records random amplitude noise on the laser beam. The final section of the trace C → D is taken with the laser switched off and corresponds to detector noise at a frequency of 6 kHz. (Figure taken from Reid et al. [26].)

65

Fig. 6-5

Second harmonic scans taken through a multipass cell set for 32 m at a pressure of < 1 Torr. Trace A is taken with a 10 cm cell of SO<sub>2</sub>/N<sub>2</sub> mixture placed in the beam. Traces B and C show high sensitivity scans taken without the 10 cm cell. Several SO<sub>2</sub> lines are observed in trace B with a typical absorption coefficient of  $\sim 2 \times 10^{-6} \text{ m}^{-1}$ . Sensitivity is limited by optical fringes. For trace C, the phase of the lock-in amplifier was set at  $\theta + 90$  where  $\theta$  was the phase used to produce the upper traces. The phase  $\theta$  had been set to give maximum P value of the 2f line-shape.

68

Fig. 6-6

Several diode laser scans taken every 60 sec with a time constant of 0.3 sec. The optical fringes observed between 618 mA and 622 mA changed slowly as the optical pathlengths in the system fluctuated. A typical fluctuation can be seen at the point A.

70

Fig. 6-7

Diode scans of  $2f$  signal as a function of time for a fixed diode current value. The traces were recorded simultaneously in phase  $\theta$  and in quadrature  $\theta + 90$  for a 1 sec and 10 sec time constant. Note the increase in the ratio of fringe noise to random beam noise as the time constant increases.

72

Fig. 6-8

Repeat of Fig. 6-7, but with a time constant of 100 sec.

73

LIST OF TABLES

		<u>Page</u>
Table 1-1	Standard deviations of $C^{14}$ measurements in an ideal counter as a function of sample size.	3
Table 4-1	List of lines in normal $CO_2$ which overlap and interfere with $C^{14}O_2$ P-branch lines.	42
Table 5-1	Calculated reduction in interference on cooling the $CO_2$ sample.	53
Table 6-1	LAS sensitivity to $C^{14}O_2$ at 195 K and 14 Torr.	76

## CHAPTER 1

### INTRODUCTION

Radiocarbon dating is possible because a minute concentration of the radioactive isotope  $C^{14}$  is present in all living plants and animals. The ratio of the concentration of the  $C^{14}$  atoms to  $C^{12}$  atoms is approximately  $10^{-12}$ . This ratio represents the atmospheric equilibrium formed between the radioactive decay of  $C^{14}$  and the production of  $C^{14}$  from  $N^{14}$  by cosmic ray neutrons. When a living object is taken out of equilibrium with the biosphere (i.e., when it dies) the concentration of  $C^{14}$  decays with a half life of 5730 years. Thus at time  $t$  years after death, the  $C^{14}$  concentration,  $N$ , is given by:

$$N = N_0 \exp(-t/8730) \quad (1-1)$$

where  $N_0$  is the value of  $N$  when death occurred (at  $t=0$ ). Experimentally, the concentration is determined by measuring the disintegration activity per gram of natural carbon. The measurement of the disintegration activity is made by conventional radiocarbon techniques, typically by oxidizing the carbon to  $CO_2$  and counting the number of decays in a proportional counter. The volume of the counter is generally several litres and it is filled to a pressure of 1 to 2 atmos-



pheres. Thus, the mass of carbon required is at least 1 to 2 gm. This mass of modern carbon will give 15-30 counts per minute. With good shielding the background count rate can be reduced to one tenth of this.

The relationship between sample size and accuracy in carbon-14 dating can be illustrated by calculating the relative error for a series of samples of different sizes. Let us consider an ideal counter registering every decay with zero background counts. Since the initial decay rate for modern carbon is approximately 15 disintegrations per minute per gram, such a counter would register about 19,600 decays in 24 hours. Therefore, the statistical counting error for a 1 gm sample is about 0.7%, which corresponds to a carbon-14 age error  $\Delta t$  of about 60 years. Table 1-1 shows the relative error for different sample sizes [1]. Notice that the error increases rapidly as the size of the sample decreases. In fact, a real counter is not 100% efficient and suffers from background counts. Hence, in a practical system the standard error for 0.01-gm sample is infinite. Therefore, conventional techniques are constrained to use several grams of carbon with a counting time of 24 to 48 hours to achieve a reasonably accurate estimate of the age of the sample.

The main disadvantage of the counting technique is the use of the tiny fraction of the atoms which decay during the counting period. In this thesis, we investigate an alternative approach to radiocarbon dating. The chief advantage of

Table 1-1

STANDARD DEVIATIONS OF  $C^{14}$  MEASUREMENTS IN AN IDEAL  
COUNTER AS A FUNCTION OF SAMPLE SIZE (Rounded figures)

SAMPLE SIZE (GRAMS)	n; CALCULATED NUMBER OF COUNTS IN 24 HOURS	$\sqrt{n}$	$\frac{1}{\sqrt{n}}$ ( $\Delta n$ )	$\Delta t$ IN YEARS
10	195,800	442	.002	20
5	97,900	312	.003	30
1	19,600	139	.007	60
0.5	9,800	98	.010	80
0.2	3,900	62	.016	130
0.1	1,950	44	.023	180
0.01	190	13	.071	600

Data taken from N.J. Van der Merwe [1].

our new technique is that it involves the detection of all the  $C^{14}$  atoms remaining in the sample. We propose to use infrared absorption to detect  $C^{14}$ . The  $C^{14}$  atoms are converted to  $CO_2$  and one then detects the radiocarbon by measuring absorption on the strong fundamental vibrational-rotational lines of  $C^{14}O_2$  near 4.5  $\mu m$ . Conceptually, it is a very simple technique. All that is required is the ability to measure the absorption of  $C^{14}O_2$  with sufficient sensitivity. In the spectral region of  $C^{14}O^{16}_2$  one has to deal with interfering absorption lines due to the more abundant isotopic species of  $CO_2$ . Part of this thesis describes an investigation of the problem of these interferences. To be a viable dating method, the infrared technique must have very high resolution to separate the  $C^{14}O_2$  lines from the other isotopic lines. In addition, the technique must be able to measure infrared absorption coefficients in the range of  $10^{-9} m^{-1}$ . To achieve the required resolution and sensitivity we use a tunable diode laser as our infrared source, in conjunction with a multipass optical cell.

The experimental apparatus is described in detail in the next chapter, where we also introduce the second harmonic detection techniques used to attain high sensitivity. Chapter 3 describes a detailed experimental investigation of these modulation techniques, and their comparison with theory. Very good agreement between theory and experiment is found. This enables one to select the optimum operating conditions for the system to obtain best signal-to-noise ratio, SNR, and the

minimum interferences. In Chapter 4 we report a detailed spectroscopic investigation of the  $\nu_3$  band of  $C^{14}O_2$ . In particular, the P branch of  $C^{14}O^{16}O_2$  was investigated line-by-line to determine the best lines for detection. The lines were evaluated by observing the absorption spectrum of natural  $CO_2$  enriched with  $C^{14}O_2$ . A search was made for those  $C^{14}O_2$  lines which suffered minimum interference from the more abundant stable isotopes of  $CO_2$ . Once the best lines had been selected, these lines were further investigated to determine the effect of cooling the gas on the interferences. These results are described in Chapter 5, and are extremely encouraging. We are confident that the detection of  $C^{14}O_2$  in a cooled multipass cell will not be limited by interferences from the stable isotopic forms of  $CO_2$ .

In the final part of this thesis, we investigate the sensitivity which can be attained with the present form of the apparatus, and compare this sensitivity with that required for practical radiocarbon dating. The experimental results are confined to a small multipass cell and short time constants. However, we can extrapolate our results to longer cells and measurement times of several hours. These extrapolations confirm that radiocarbon dating by infrared absorption is feasible, and may well be superior to conventional counting techniques, in that a smaller carbon sample is required.

Throughout this thesis we have chosen to compare the laser absorption technique to conventional beta activity measurement techniques. Recently, very impressive results on  $C^{14}$  detection have been achieved using accelerators [2]. This is another method for direct detection of the  $C^{14}$  remaining in the sample, and the accelerators achieve high sensitivity with very small samples. The chief drawback appears to be the expense and limited availability of dedicated accelerators [2].

## CHAPTER 2

### EXPERIMENTAL APPARATUS AND DETECTION TECHNIQUES

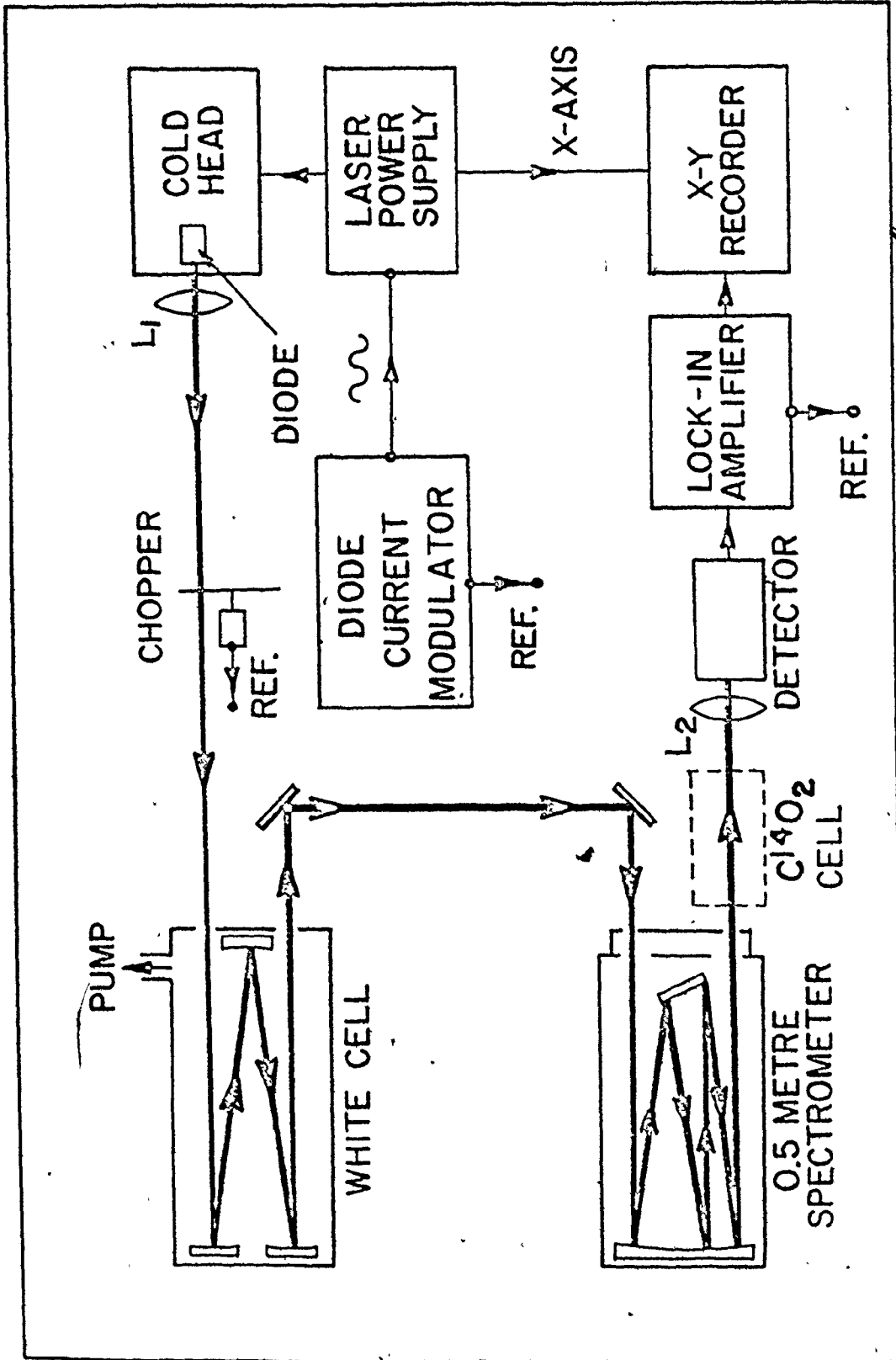
#### 2.1 Experimental Apparatus

The initial form of the apparatus used in the experiments is illustrated schematically in Fig. 2-1. A wavelength tunable lead-salt diode laser is used in conjunction with a multipass cell. The diode laser was supplied by Laser Analyt-ics Inc. The diode is mounted on a copper tip in a vacuum chamber, and cooled by a cryogenic He refrigerator. The coarse adjustment of the laser wavelength is carried out by varying the temperature of the diode from 10 to 60 K. For the particular diode used in the experiment, this gives a spectral coverage from 2100 to 2300  $\text{cm}^{-1}$ . The fine adjustment of wavelength is obtained by varying the drive current supplied to the diode. The diode laser tends to operate at several different wavelengths (longitudinal modes) simultaneously. A 0.5 m spectrometer is used to select one of these wavelengths. In general, the diode can be tuned continuously over  $\sim 1.5 \text{ cm}^{-1}$ . The typical tuning rate of the diode is  $40 \text{ cm}^{-1}/\text{A}$ . If required, single mode operation of the diode can be obtained by maintaining the diode current near threshold. Typical powers in the individual diode modes are 100 to 200  $\mu\text{W}$ .

The laser output is collected by a 5 cm focal length

Fig. 2-1

Schematic diagram of the apparatus used for a line-by-line investigation of the  $\nu_3$  band of  $C^{14}O_2$ . Strong absorption lines were measured using the chopper and direct detection, but second harmonic modulation techniques were employed to measure weak absorption lines [3].





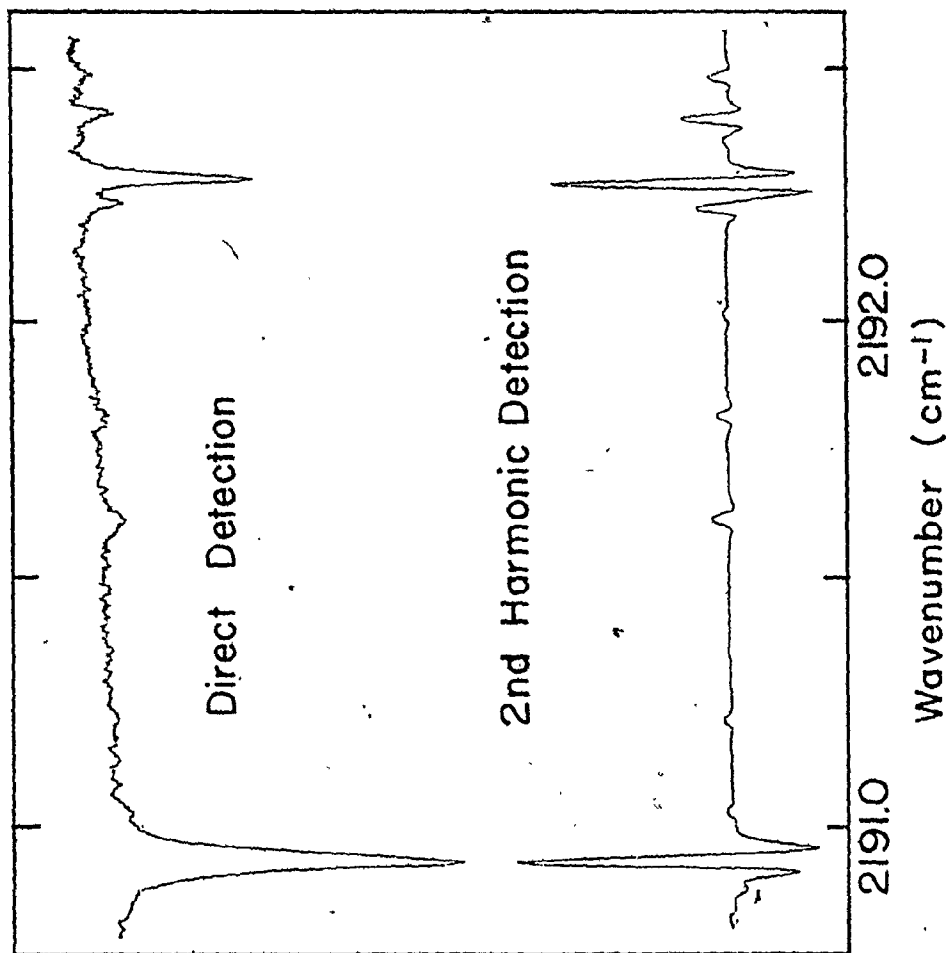
lens, and focused into a 5 m base-pathlength multipass cell. The output beam from the multipass cell passes through the spectrometer and is then focused onto a HgCdTe detector. For direct detection of infrared absorption lines an external chopper and a lock-in amplifier are used to synchronously detect the output power from the laser. An X-Y recorder is used to plot the laser power against diode current. (in general, the diode laser wavelength varies linearly with diode current). We typically used an optical pathlength of 200 m in the multipass cell. To investigate the spectrum of CO<sub>2</sub>, the cell was filled with 30 Torr of Coleman grade CO<sub>2</sub> (Matheson). The upper trace of Fig. 2-2 shows a typical diode laser scan taken through 200 m of CO<sub>2</sub>. The diode tunes over the spectral region near 2192 cm<sup>-1</sup>, and several absorption lines can be seen in direct detection. The noise visible on the upper trace results from power fluctuations as the position of the laser beam passes through the narrow spectrometer slits.

## 2.2 Second Harmonic Detection

Direct detection, as shown in the upper trace in Fig. 2-2, does not allow high sensitivity measurements of infrared absorption lines. Power fluctuations limit the sensitivity. A much more sensitive technique employs wavelength modulation of the diode laser, with synchronous detection at twice the modulation frequency [3]. For convenience, we will refer to the second harmonic detection technique as 2f detection.

Fig. 2-2

$\text{CO}_2$  spectrum taken through 200 m pathlength at a pressure of 30 Torr. The upper trace shows an absorption spectrum obtained with direct detection. The lower trace was taken with second harmonic detection. Notice the substantial increase in signal-to-noise ratio obtained by switching from direct to second harmonic detection.



e

The lower trace in Fig. 2-2 shows the results of using this 2f technique. An external generator modulates the diode current at 3 kHz, while the lock-in amplifier synchronously monitors the signal at 6 kHz. A digital voltmeter is used to monitor the amplitude of the external modulation. Note the improved signal-to-noise ratio (SNR) in the lower trace, and the type of lineshape obtained with 2f detection. Chapter 3 deals in detail with these lineshapes, and their dependence on parameters such as modulation amplitude and gas pressure.

## CHAPTER 3

### MODELLING OF THE SECOND HARMONIC TRANSFER FUNCTION

#### 3.1 Introduction

The 2f detection technique described briefly at the end of chapter 2 is used extensively throughout the work reported in this thesis to obtain very high sensitivity. To fully understand this detection technique, and to enable us to optimize parameters such as modulation amplitude and gas pressure, we have made a detailed comparison between theory and the experimental 2f lineshape. This chapter presents the details of calculations of the 2f lineshape for a Lorentzian and Doppler broadened absorption line, and compares the theoretical lineshape with some experimental results.

Harmonic detection has been used almost universally in experimental studies of weak nuclear magnetic resonance (NMR) and electron paramagnetic resonance (EPR) signals [4]. The model presented here is based on the calculations of Arndt [5], who gives a simple, closed, general analytic solution for all the Fourier coefficients of a Lorentzian lineshape. We find very good agreement between theory and experiment for a wide range of modulation amplitude. A Lorentzian lineshape formulation is suitable for absorption lines in CO<sub>2</sub>

at a pressure greater than 30 Torr. However, in the present series of experiments we wish to maximize the absorption coefficient for a given line while minimizing the interference between adjacent lines. This calls for working not with Lorentzian lineshapes, but with lineshapes represented by a Voigt profile. Hence, we have investigated the variation of direct absorption and 2f signal as a function of pressure in the region from 40 Torr to 2 Torr. Once again, good agreement is found between theory and experiment. This enables us to systematically optimize gas pressure and modulation amplitude in the later parts of the experimental work.

### 3.2 Mathematical Model of the Harmonic Detection Technique

The intensity  $I(\nu)$  at frequency  $\nu$  of an electromagnetic wave passing through a cell of length  $L$  filled with a gas is given by:

$$I(\nu) = I_0(\nu) e^{-\alpha(\nu)L} \quad (3-1)$$

where  $I_0(\nu)$  is the incident intensity and  $\alpha(\nu)$  is defined as the absorption coefficient. In the case of interest,

$$\alpha(\nu)L \leq 0.05 \quad (3-2)$$

hence,

$$I(\nu) \approx I_0(\nu) [1 - \alpha(\nu)L] \quad (3-3)$$

The absorbed intensity at frequency  $\nu$ ,  $I_{ab}(\nu)$ , is:

$$I_{ab}(\nu) = I_0(\nu) - I(\nu) \quad (3-4)$$

$$= I_0(\nu)\alpha(\nu)L. \quad (3-5)$$

If we consider an isolated absorption line in a gas at a pressure high enough to ensure that pressure broadening dominates (for  $\text{CO}_2$ ,  $P > 30$  Torr), then  $\alpha$  is described by a Lorentzian function

$$\alpha(\nu) = \frac{\alpha_0}{1 + \left(\frac{\nu - \nu_0}{\Delta\nu}\right)^2} \quad (3-6)$$

where  $\Delta\nu$  is the half width at half maximum (HWHM) of the absorbing line,  $\alpha_0$  is the absorption coefficient at line centre, and  $\nu_0$  is the transition frequency. To produce the harmonic line-shape using the diode laser, a sinusoidal modulation of frequency,  $\omega$ , and amplitude,  $a$ , is superimposed upon the diode current. This results in a modulation in time  $t$  of the diode frequency given by the following expression

$$\nu = \bar{\nu} + a \cos \omega t. \quad (3-7)$$

The mean frequency,  $\bar{\nu}$ , is slowly tuned by ramping the diode current. We assume that the incident diode power does not

vary over the line, i.e.,

$$\begin{aligned} I_o(\bar{\nu}) &= I_o(\nu_o) \\ &= I_o . \end{aligned} \quad (3-8)$$

Let us define two dimensionless parameters;

$$x \equiv \frac{\bar{\nu} - \nu_o}{\Delta\nu} \quad (3-9)$$

$$m \equiv \frac{a}{\Delta\nu} . \quad (3-10)$$

The absorption coefficient becomes

$$\alpha(x,m) = \frac{\alpha_o}{1+(x+m \cos \omega t)^2} . \quad (3-11)$$

Hence, the absorbed intensity is:

$$I_{ab}(x,m) = I_o \alpha(x,m) L . \quad (3-12)$$

The calculation of each Fourier component of the absorption coefficient has been carried out by Arndt [5]. The result is:

$$\alpha(x,m) = \alpha_o \sum_{n=0}^{\infty} S_n(x,m) \cos n \omega t , \quad (3-13)$$

$$S_n(x,m) = \frac{1}{2} \frac{1}{m^n} \epsilon_n \frac{i^n \{ [(1-ix)^2 + m^2]^{\frac{1}{2}} - (1-ix) \}^n}{[(1-ix)^2 + m^2]^{\frac{1}{2}}} + c.c. \quad (3-14)$$

where  $\epsilon_o = 1$

$$\epsilon_n = 2, \quad n = 1, 2, \dots .$$



Le Naour et al. [6] have obtained the same result by using contour integration.

The 2f lineshape is given by the coefficient of the Fourier series with  $n=2$ . After some algebraic manipulations, this can be written as:

$$S_2(x, m) = \frac{4}{m^2} - \frac{2^{1/2}}{m^2} \frac{(M+1-x^2) [(M^2+4x^2)^{1/2} + M]^{1/2} + 4x[(M^2+4x^2)^{1/2} - M]^{1/2}}{(M^2+4x^2)^{1/2}} \quad (3-15)$$

where  $M = 1-x^2+m^2$ .

In the upper part of Fig. 3-1, we display calculated 2f lineshapes for typical values of  $m$ . In the lower part of Fig. 3-1 we show the experimental 2f lineshape for the same value of the dimensionless parameter  $m$ . (Details of the experimental techniques are given in the next section). Clearly, there is good qualitative agreement between theory and experiment.

### 3.3 Comparison Between Theory and Experiment

The apparatus used to investigate the 2f lineshape is essentially the same as shown on Fig. 2-1. However, the spectrometer is removed from the beam, and the diode is operated in a single mode. We arrange for the diode laser to tune over a suitable isolated absorption line in gases such as  $\text{CO}_2$ ,  $\text{SO}_2$  or  $\text{NO}$ . The pathlength in the gas is chosen to ensure that the peak absorption is  $\leq 5\%$  and the gas pressure is generally varied from 2 to 40 Torr. In these experiments we have used three different diode lasers, showing that the results obtained are not specific to a particular diode.

Fig. 3-1

Qualitative comparison between theory and experiment for the 2f lineshape. Note the broadening of the lineshape as the modulation amplitude is varied. As shown in the Figure, the positive part, P, and the negative part, N, of the 2f lineshape are defined as the maximum positive and the maximum negative excursion of the 2f lineshape from the baseline. The ratio, R, is defined as  $R \equiv P/N$ .

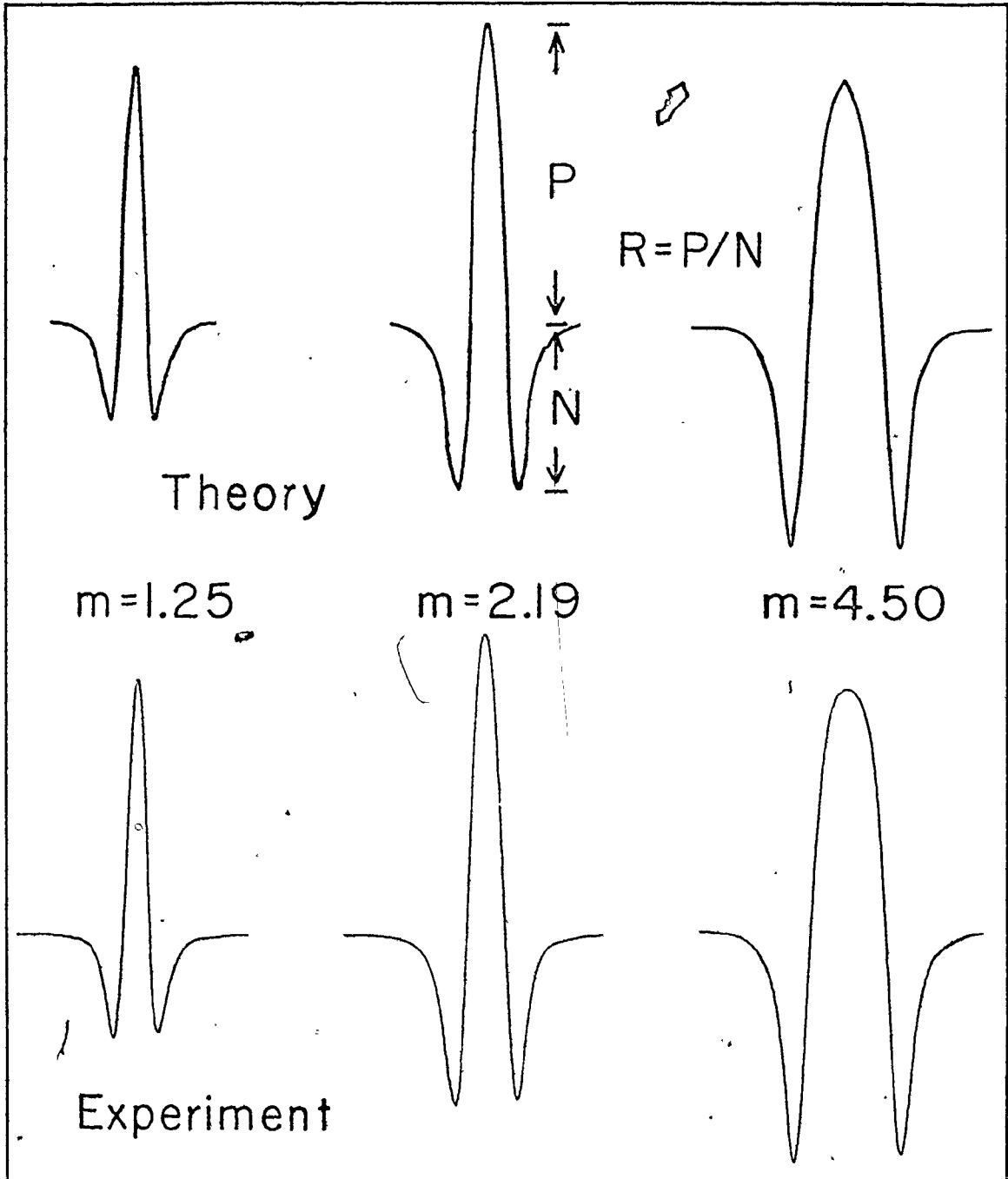


Figure 3-1 shows good qualitative agreement between theory and experiment. The experimental lineshape has the expected behavior as  $m$  increases. The width increases as  $m$  increases and both theoretical and experimental curves have the same relative magnitude as  $m$  is varied. To perform a quantitative comparison between theory and experiment, we have chosen to examine some particular parameters of the  $2f$  lineshape. We chose to look specifically at two parameters of the  $S_2(x,m)$  function: The value of the positive part,  $P$ , and the value of the ratio of the positive to the negative part,  $R$ . Experimentally this ratio  $R$  is very convenient as it can be measured directly from the X-Y recorder traces without calibration of either the X or the Y axis, and the ratio does not depend upon the laser power. We have plotted the ratio  $R$  as a function of the input modulation amplitude,  $A$ , as measured with a digital voltmeter. Typical results are plotted on Fig. 3-2. Figure 3-2 shows the results taken at two different frequencies of modulation. The measurements were made on an absorption line which had a pressure broadened linewidth 2.6 times the Doppler linewidth. Thus the lineshape closely approximates a true Lorentzian. Care was taken to ensure that the  $2f$  lineshape was not distorted by the time constant of the lock-in amplifier. Typical error bars on  $R$  are indicated on several data points. Also shown in Fig. 3-2 is a theoretically calculated curve of  $R$  as a function of  $m$ . To display these curves we have assumed that

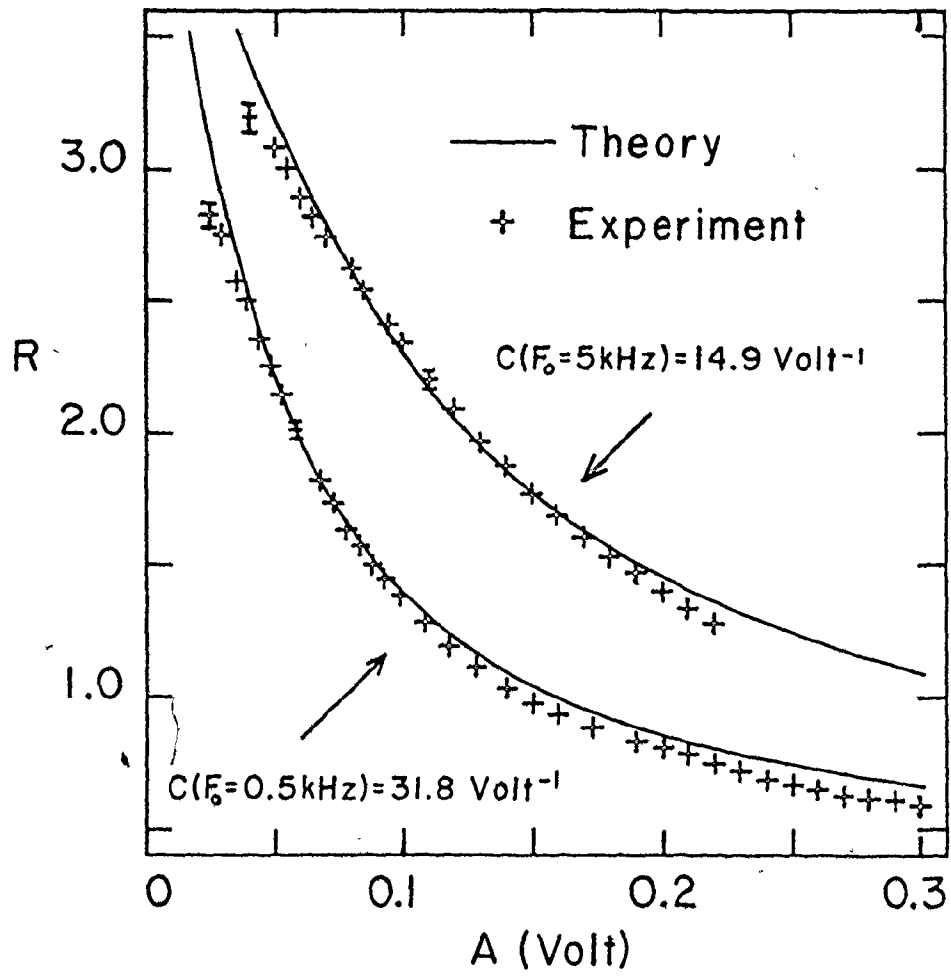


Fig. 3-2

Plot of the ratio  $R$  as a function of the modulation amplitude  $A$  for two values of the modulation frequency. Also shown are the theoretical curves fitted to the experiment assuming a linear relationship between the wavelength modulation  $m$  and  $A$ .

the wavelength modulation amplitude  $m$  is proportional to the applied current modulation  $A$ . Clearly the good agreement over the entire range of  $A$  confirms that  $m$  is indeed proportional to  $A$ . While the overall agreement between theory and experiment is very good, there is a slight discrepancy at both low and high modulation amplitude. Later we will show that the discrepancy at low values of  $m$  can be explained by the slight departure of the experimental lineshape from a pure Lorentzian. At very large values of  $m$ , the output of the diode laser becomes distorted and can no longer be exactly represented by 3-7 and 3-8. Nevertheless, the results shown in Fig. 3-2 clearly demonstrates that the wavelength modulation  $m$  is proportional to the applied current modulation  $A$  over the range of interest in the present series of experiments.

We investigated the variation of the scaling coefficient,  $C$ , given by:

$$C = M/A$$

as a function of the applied frequency of modulation. This coefficient is expected to decrease as the frequency of modulation increases due to the thermal time constant involved in the diode tuning mechanism. Experimental results confirm this (see Fig. 3-2, for example). We found that the scaling factor  $C$  decreases by a factor of 2.1 when the frequency of

modulation  $F_0$  increases from 0.5 to 5.0 kHz. A knowledge of the variation of  $C$  with  $F_0$  allows us to choose the optimum frequency of modulation.

The results shown in Fig. 3-2 enable us to relate the  $A$  values to the  $m$  values. Having determined  $m$ , we can now plot experimental values of  $P$  as a function of  $m$ , and compare these with theory. Typical results are shown in Fig. 3-3. For each data point, the value of  $P$  measured on the X-Y recorder was normalized to the total diode power. Once again typical error bars are shown. Also shown on Fig. 3-3 is the theoretical variation of  $P$  as a function of  $m$ . To compare the theoretical relationship with the experimental points the maximum value of each graph is set at unity. There is good agreement over the entire range of modulation amplitudes. As a final check we carried out a quantitative comparison between an experimental and calculated lineshape. Figure 3-4 shows the very good agreement obtained for all values of  $x$ .

So far we have only dealt with the relative amplitude of the  $2f$  lineshape. Good agreement is seen in the relative lineshape, but we have always used a scaling factor when comparing theory and experiment. We have investigated the absolute relationship between the magnitude of an isolated line measured directly, and the signal obtained with  $2f$  detection. To carry out this comparison, the absorption line is first measured employing direct detection with a chopper in the



Fig. 3-3

Plot of the positive part of the  $2f$  lineshape,  $P$  as a function of  $m$  for both theory and experiment. The maximum value of  $P$  is normalized to 1. The experimental  $A$  values are fitted to the  $m$  values using the scaling factor determined from the ratio measurements.

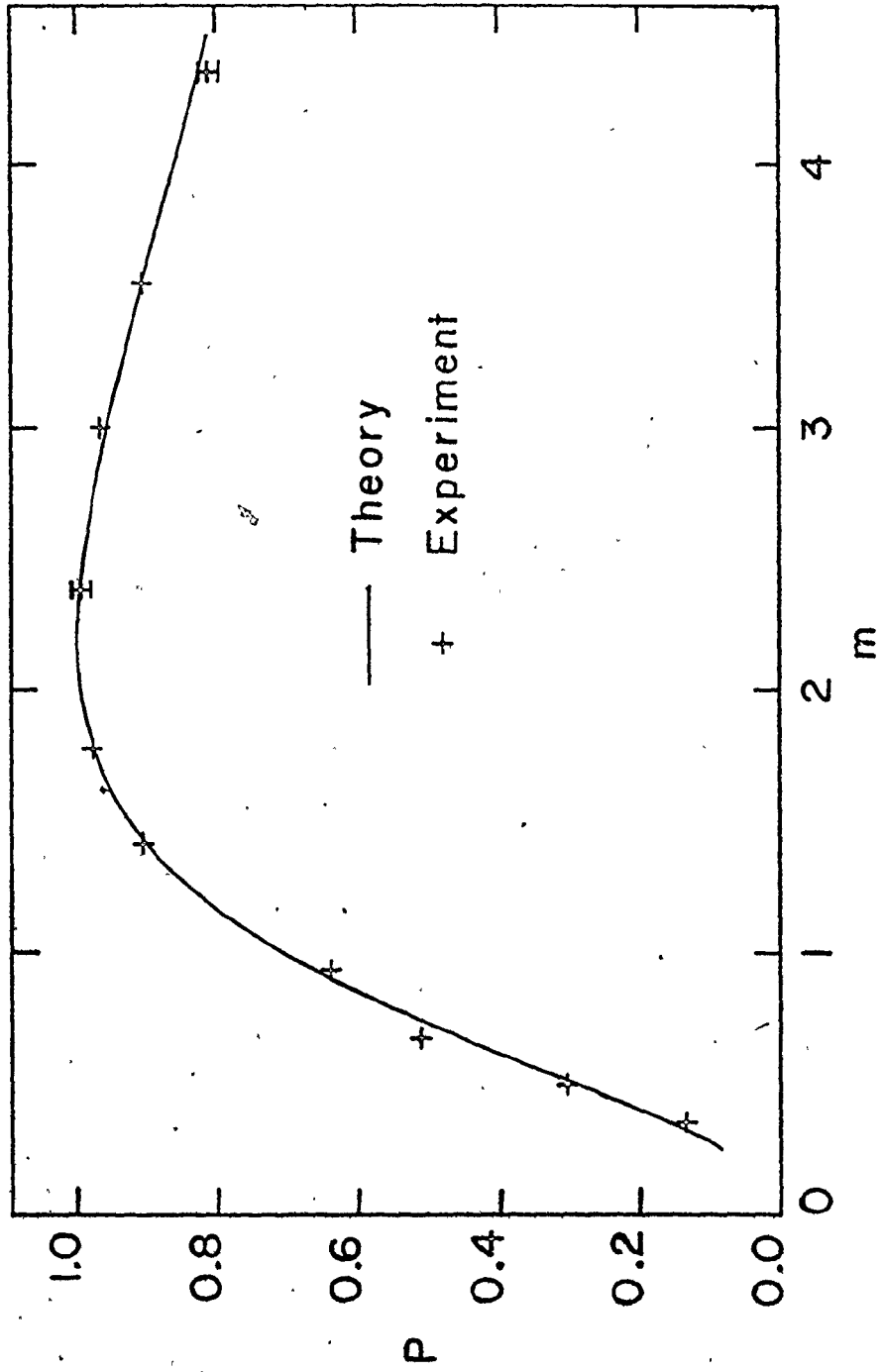
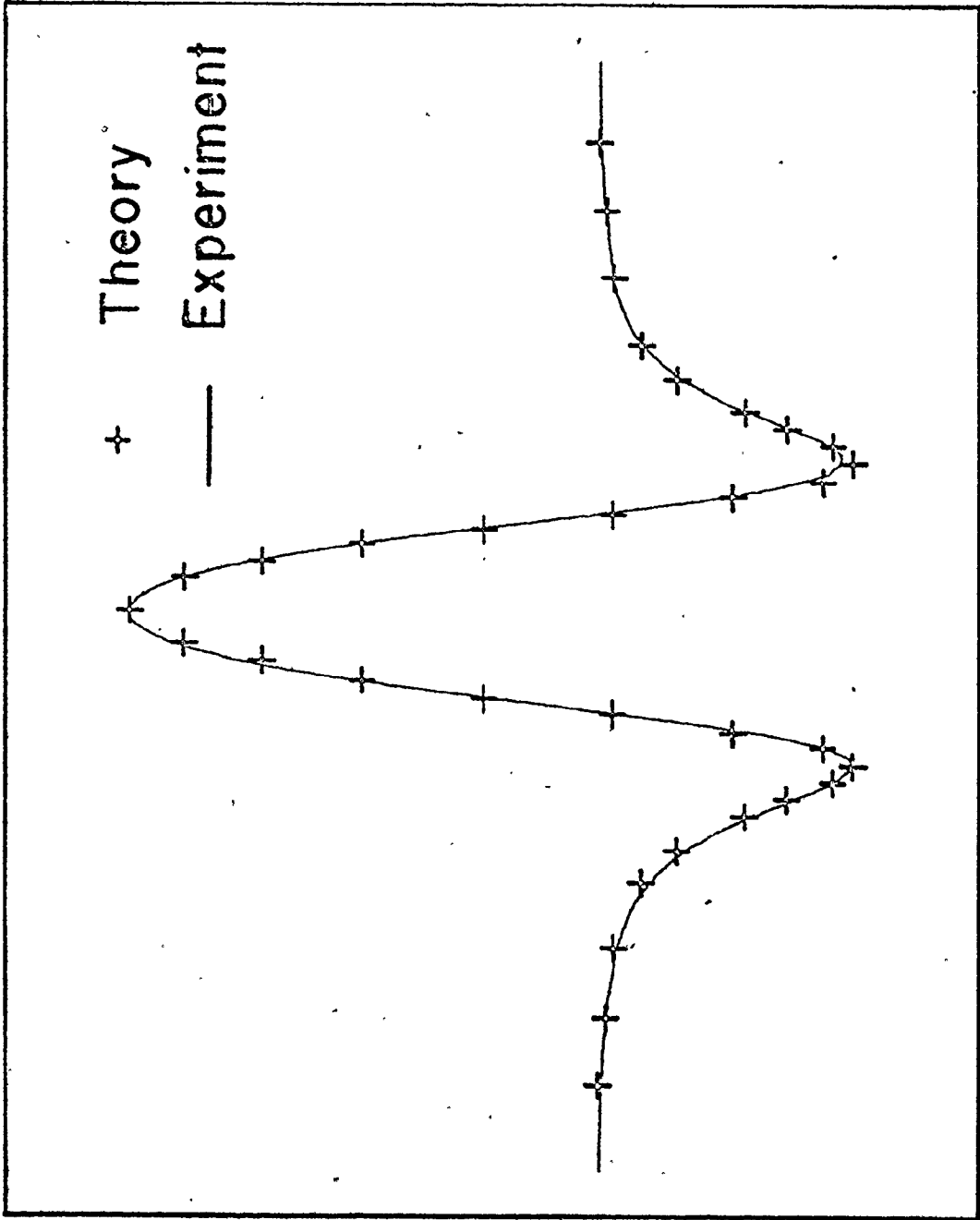


Fig. 3-4

Scan of the  $2f$  lineshape as a function of wavelength for  $m = 2.2$ . The experimental curve is taken from the X-Y recorder trace, while the theory is adjusted to fit by using a single scaling factor for each axis.



Current

2nd Harmonic Signal

+ Theory  
— Experiment

beam. The chopper is then removed and the  $2f$  lineshape signal is obtained with the modulation amplitude set at  $m = 2.2$  to give the optimum value of  $P$ . We found that the ratio of the magnitude of  $P$  to the magnitude of the direct signal lies between 0.5 and 0.6. This compares with a theoretical value of 0.343. However, the theoretical calculation does not take into account the fact that the mechanical chopper blocks the laser beam for 50% of the time. Thus the  $2f$  lineshape is measured with an average laser power which is double that employed in direct detection. Consequently, the ratio of  $2f$  signal to direct signal is approximately twice that predicted by the theory of Arndt [5]. This is an important point as it ensures that by switching to  $2f$  detection, we actually lose very little signal.

In the next section, we investigate the variation of the  $2f$  signal as the pressure of the absorbing line is reduced from the pressure broadening region through the region where the Voigt profile holds, down to the Doppler region.

### 3.4 Dependence of the $2f$ Lineshape upon Gas Pressure

In the previous section of this chapter, we have shown good agreement between experiment and theory when the absorption line is described by a Lorentzian function. However, for the detection of radiocarbon we wish to operate at

a lower pressure to minimize the linewidth of the individual lines, and hence minimize the interferences. For an isolated absorption line in  $\text{CO}_2$ , we investigated the variation of the absorption coefficient, and the  $2f$  signal, for gas pressure between 2 and 40 Torr.

Figure 3-5(a) shows the absorption coefficient as a function of pressure, as measured directly using an external chopper. As expected, the absorption coefficient increases until the gas becomes almost pressure broadened around 40 Torr, where the absorption coefficient is expected to be constant independent of pressure. The solid curve shown in Fig. 3-5(a) is a calculated fit to an absorption line described by a Voigt profile with the following parameters:

$$\begin{aligned} \Delta\nu_L &= 3.3 \text{ MHz/Torr,} \\ \Delta\nu_D &= 61.1 \text{ MHz corresponding to } T = 298 \text{ K} \\ S &= 1.077 \times 10^{-24} \text{ cm}^{-1}/(\text{mol.cm}^{-2}) \end{aligned}$$

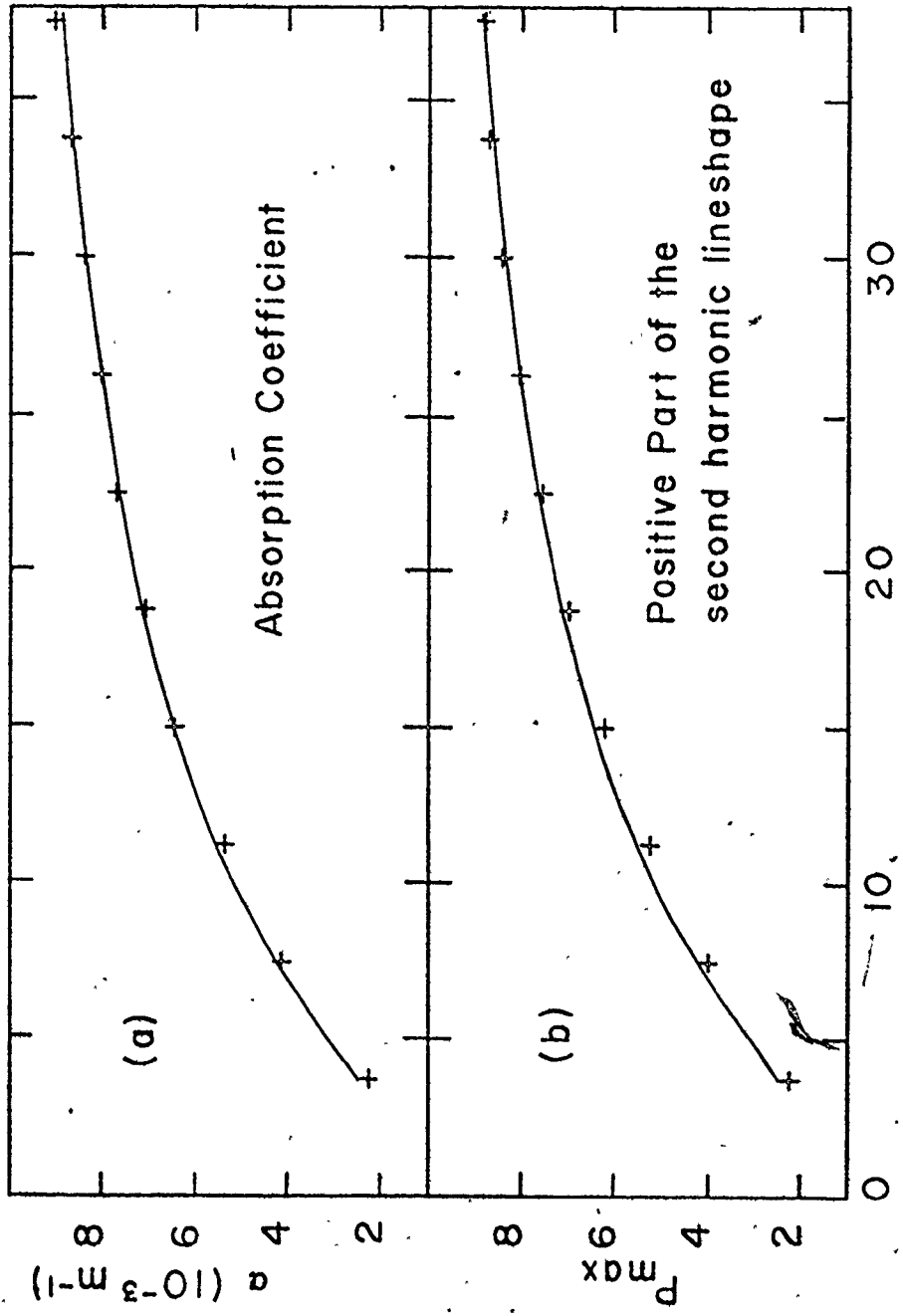
where the subscripts L and D stand for Lorentzian and Doppler respectively, T is the gas temperature and S is the integrated intensity.

Once we had determined the variation of the absorption coefficient with pressure, we investigated the effect of gas pressure on the  $2f$  lineshape. For each gas pressure, the modulation amplitude was adjusted to maximise the positive part P. The resultant plot of  $P_{\text{max}}$  versus pressure is given in Fig. 3-5(b).

Fig. 3-5

(a) Absorption coefficient as a function of pressure for the vibrational-rotational transition P(56)  $02^{\circ}0 \rightarrow 02^{\circ}1$  of  $C^{13}O^{16}_2$ . An absorption line described by a Voigt function is fitted to the experiment with a pressure broadening coefficient of 3.3 MHz/Torr and an integrated intensity of  $1.077 \times 10^{-24} \text{ cm}^{-1}/(\text{mole, cm}^{-2})$ .

(b) Plot of  $P_{\text{max}}$  as a function of pressure. At each pressure, the modulation amplitude was adjusted to maximize the positive part P. The experimental results are scaled to the Voigt function displayed in (a).





The calculated curve from Fig. 3-5(a) is also shown in Fig. 3-5(b), using a single scaling factor in the fit. Clearly,  $P_{\max}$  has the same dependence upon pressure as  $\alpha$ ; i.e., if the gas pressure is reduced so as to decrease  $\alpha$  by a factor of 2,  $P_{\max}$  is also decreased by 2. The results shown in Fig. 3-5 enable us to choose a pressure of  $\sim 20$  Torr as optimum for radiocarbon detection. At 20 Torr,  $P_{\max}$  is reduced by only  $\sim 25\%$  from the high pressure value, but any further decrease in pressure results in a substantial reduction in signal.

Thus far, we have carried out detailed investigations of Lorentzian lineshapes, and an empirical investigation of  $P_{\max}$  for lines represented by Voigt profiles. The 2f function of a Voigt and a Doppler profile does not have a simple analytic expression. A calculation of the 2f lineshape and signal amplitude for a Doppler absorption line by using numerical integration of the Fourier integrals was carried out by Wilson [7]. We calculated by using the same method  $P$  and  $R$  with the following equation:

$$S_2(Y,W) = \frac{2}{\pi} \int_0^{\pi} G(Y+W\cos\theta) \cos 2\theta d\theta,$$

where  $G(x) \equiv \exp(-x^2/\pi)$ ,  $\Delta\nu = (\pi \ln 2)^{1/2}$ ,  $x = Y/\Delta\nu$  and  $m = W/\Delta\nu$ . Figure 3-6 shows the calculated  $P$  value as a function of  $m$  for both Doppler and pure Lorentzian broadened lines. Each graph is normalised to a maximum value of 1. Also shown on

Fig. 3-6

Calculated P value as a function of m for both pure Doppler and pure Lorentzian broadened lines. The maximum value of each graph is normalised to 1. Also shown are experimental data points obtained with a line which is almost entirely Doppler broadened (the ratio of the Doppler linewidth to the pressure broadened linewidth is 8).

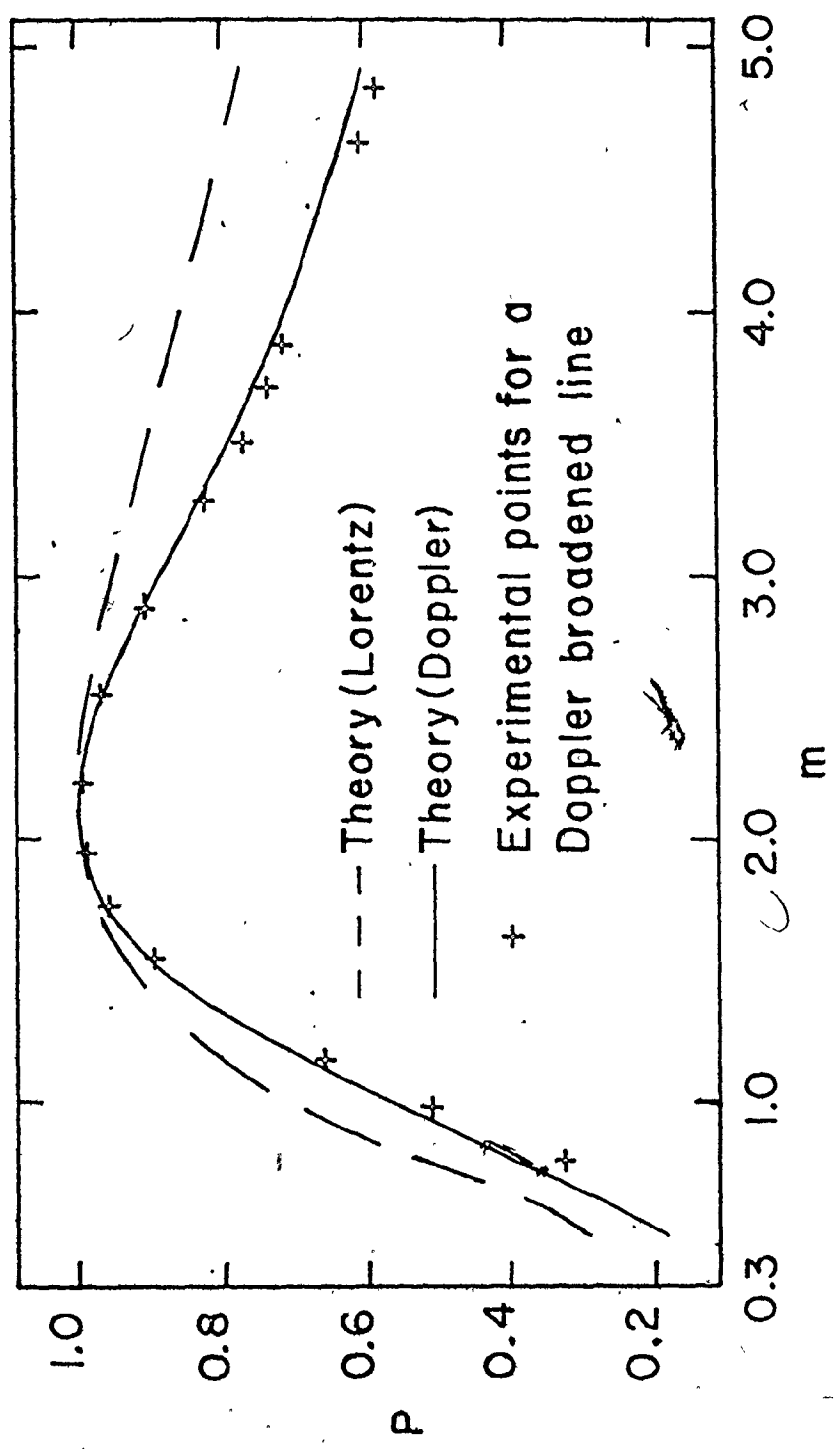


Fig. 3-6, are experimental data points obtained at a pressure of 2.4 Torr. The measurements were made on an absorption line which had a Doppler linewidth 8.0 times the pressure broadened linewidth. Good agreement exists between theory and experiment over the entire range of modulation. Note that the  $m$  value corresponding to  $P_{\max}$  is the same for both lineshapes. Figure 3-7 is a plot of the calculated ratio  $R$  as a function of  $m$  for both lineshapes. Also shown is the measured ratio  $R$  for the predominantly Doppler-broadened line. Note the slight deviation from the pure Doppler curve at low modulation amplitude. We interpret this deviation as being caused by the small pressure broadened component of our experimental lineshape. Similarly, the discrepancy between theory and experiment observed at low  $m$  values in Fig. 3-2 results from an experimental absorption line which is not entirely Lorentzian in lineshape. Once again, we attribute the small discrepancies observed between theory and experiment at high  $m$  values in Fig. 3-7 to slight diode distortions which make Eq. 3-7 and 3-8 no longer exact.

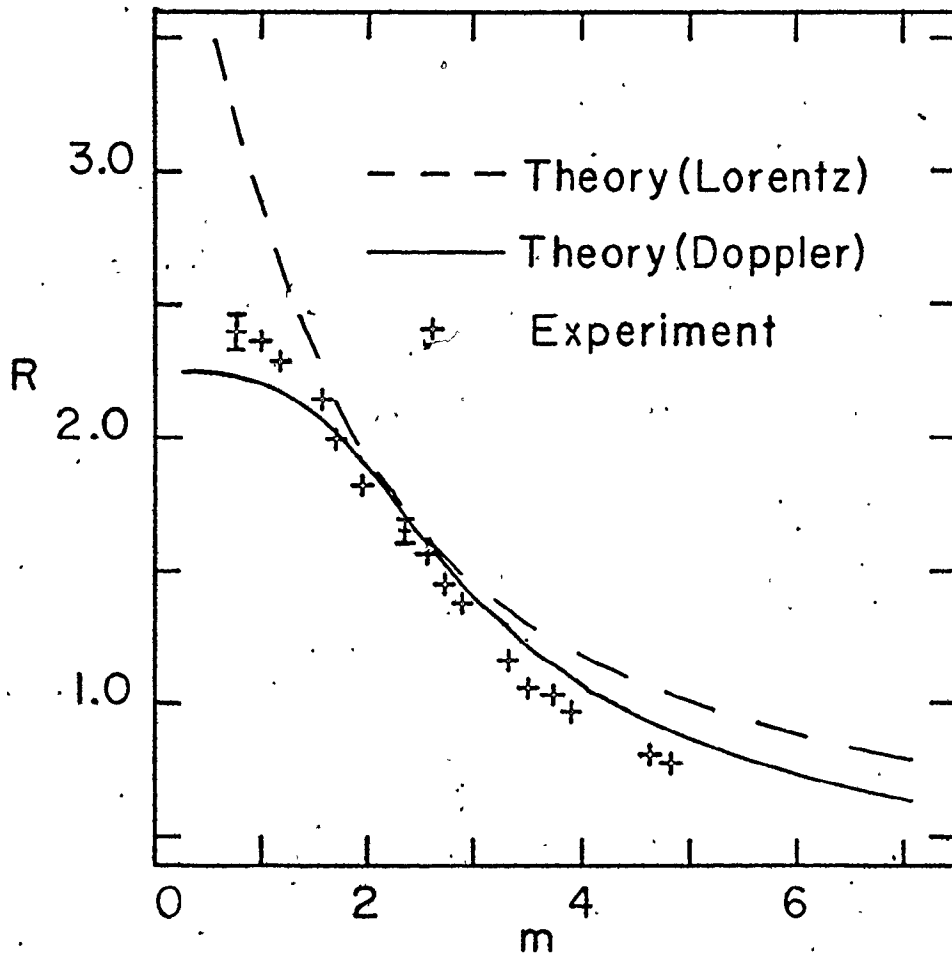
### 3.5 Conclusions

In this chapter we have carried out a detailed investigation of the  $2f$  lineshape. Our findings are summarised below:

- (a) The theoretical expressions of Arndt [5] provide an excellent description of the experimental  $2f$  lineshape

Fig. 3-7

Calculated ratio  $R$  as a function of  $m$  for both line-shapes. Also shown are the measured ratios  $R$  for the predominantly Doppler-broadened line. The measured ratios  $R$  are obtained from the  $2f$  lineshapes used to produce the results shown in Fig. 306. The scaling factor used to relate  $A$  to  $m$  in Fig. 3-6 is the same as the one employed in this Figure.



for a Lorentz absorption line.

- (b) The amplitude of the diode wavelength modulation is proportional to the externally applied modulation voltage. The constant of proportionality varies slowly with applied frequency.
- (c) The absolute magnitude of the  $2f$  signal is very similar to the magnitude of the direct signal obtained with an external chopper, i.e., there is negligible loss of signal on switching to  $2f$  detection.
- (d) In the pressure region between Doppler and Lorentz lineshapes, the optimum  $2f$  signal is proportional to the absorption coefficient.
- (e) At low pressures, the  $2f$  lineshape is well represented by the second Fourier coefficient of a frequency modulated Doppler lineshape.

The findings described above are used extensively to optimise conditions in our radiocarbon detection experiments.

## CHAPTER 4

### SPECTROSCOPY OF CO<sub>2</sub> NEAR 4.5 μm - DETAILED INVESTIGATION OF THE P-BRANCH OF THE ν<sub>3</sub> BAND OF C<sup>14</sup>O<sub>2</sub>

#### 4.1 Introduction

This chapter deals with the problem of interference between the C<sup>14</sup>O<sub>2</sub> absorption lines we wish to measure, and the many background lines belonging to the other isotopic species of CO<sub>2</sub>. A description of the absorption spectrum of CO<sub>2</sub> in the spectral region of C<sup>14</sup>O<sup>16</sup><sub>2</sub> is given in the next section. We show that the P-branch lines of the ν<sub>3</sub> band of C<sup>14</sup>O<sub>2</sub> are the best candidates for interference-free detection of radiocarbon. Section 4.3 discusses experimental results obtained for the C<sup>14</sup>O<sub>2</sub> lines, and the background spectra of normal, room temperature CO<sub>2</sub>. At room temperature, we find that even the most favorable C<sup>14</sup>O<sub>2</sub> lines are overlapped by relatively strong absorption lines.

#### 4.2 Absorption Spectrum of CO<sub>2</sub> near 4.5 μm

The CO<sub>2</sub> molecule is a triatomic linear molecule belonging to the point group C<sub>∞v</sub>. There are three normal modes of vibration, namely, symmetric stretching ν<sub>1</sub>, bending ν<sub>2</sub> and asymmetric stretching ν<sub>3</sub>, which are associated with the species Σ<sup>+</sup>, π, Σ<sup>+</sup>, respectively. Since the molecule is free to rotate, there are several rotational levels associated with



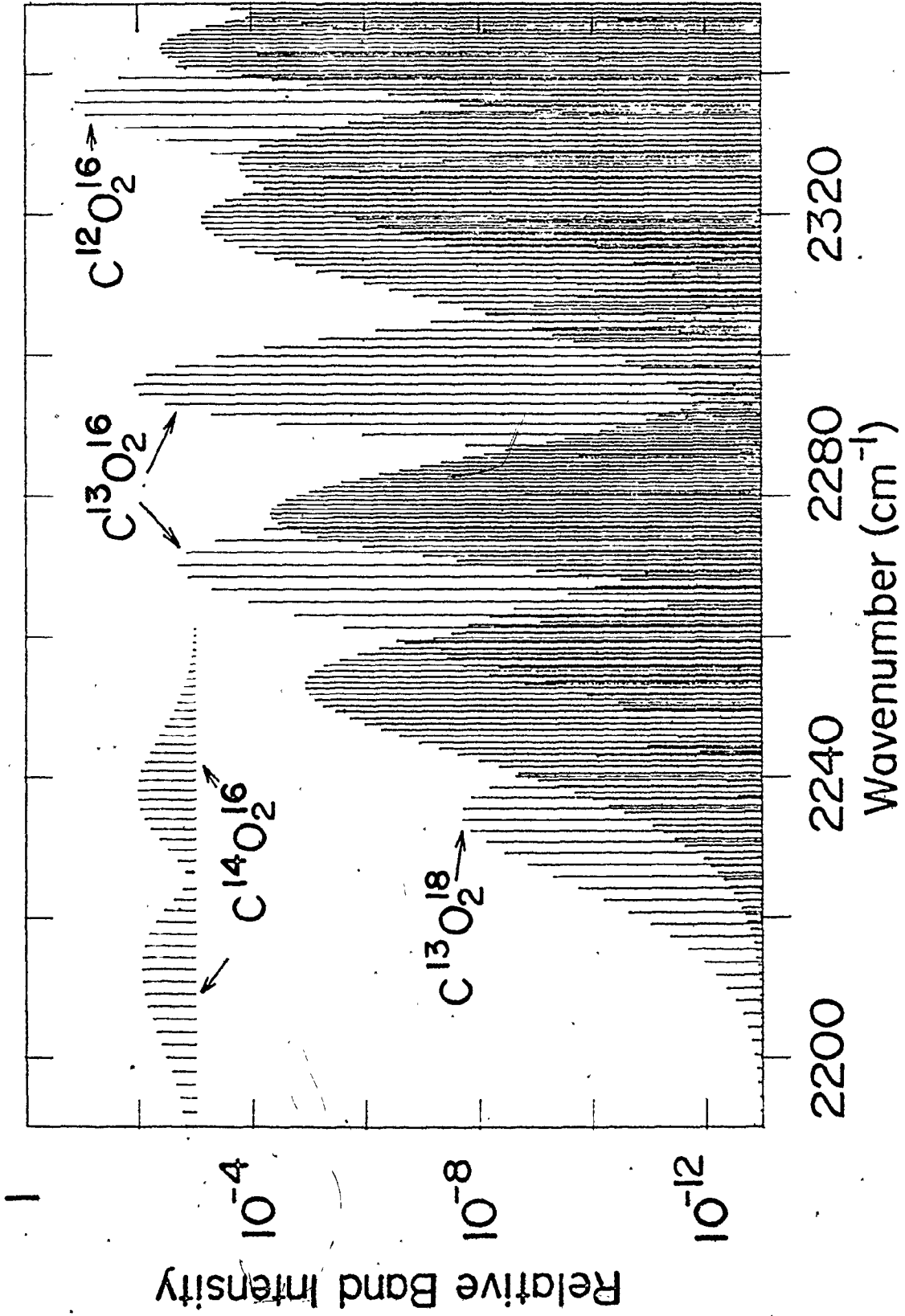
each vibrational level. We aim to detect  $C^{14}$  by measuring the absorption coefficients of the vibro-rotational transitions in the  $\nu_3$  fundamental band of  $C^{14}O^{16}_2$ .

Each vibrational level of  $CO_2$  is identified by a set of four numbers  $(n_1, n_2^\ell, n_3)$  where  $n_1, n_2, n_3$  are the vibrational quantum numbers associated with the  $\nu_1, \nu_2$  and  $\nu_3$  modes respectively, and  $\ell$  is the vibrational angular momentum. The lines observed in the 4.5  $\mu m$  spectral region are mostly caused by transitions from the  $(n_1, n_2^\ell, n_3)$  to the  $(n_1, n_2^\ell, n_3+1)$  vibrational levels. To a good approximation the absorption bands of the rarer isotopic species of  $CO_2$  have band strengths which are directly proportional to the isotopic abundance. As the relative abundance of  $C^{14}$  in a modern sample is only  $\sim 10^{-12}$ , one must therefore take into account all the isotopic forms of  $CO_2$  ( $C^{12}, C^{13}, O^{16}, O^{17}, O^{18}$ ) in evaluating the effects of interfering spectra. Consequently, we extended the calculations of McClatchey et al. [8] to include the transitions of less abundant isotopes. Expressions for the linestrengths, and the selection rules, were taken from Penner [9]. Data for the molecular constants, and expressions for the line positions, linestrengths and the linewidths are given in references [10]-[21], [8].

Figure 4-1 is a computer generated spectrum of  $CO_2$  in the 4.4  $\mu m$  region. The  $\nu_3$  fundamental bands of most of the relevant isotopic species are included. The strongest line in each band is normalized on a logarithmic scale to its

Fig. 4-1

Calculated spectrum of CO<sub>2</sub> in the 4.4 μm region. The ν<sub>3</sub> fundamental bands of most of the relevant isotopic species are included. The relative strength of each band is normalised to the C<sup>12</sup>O<sup>16</sup><sub>2</sub> bandstrength on a logarithmic scale, but the individual lines in each band are plotted in a linear fashion. The C<sup>14</sup>O<sub>2</sub> ν<sub>3</sub> band is displayed with an intensity corresponding to a modern carbon sample, (C<sup>14</sup>/C<sup>12</sup> ~ 10<sup>-12</sup>).

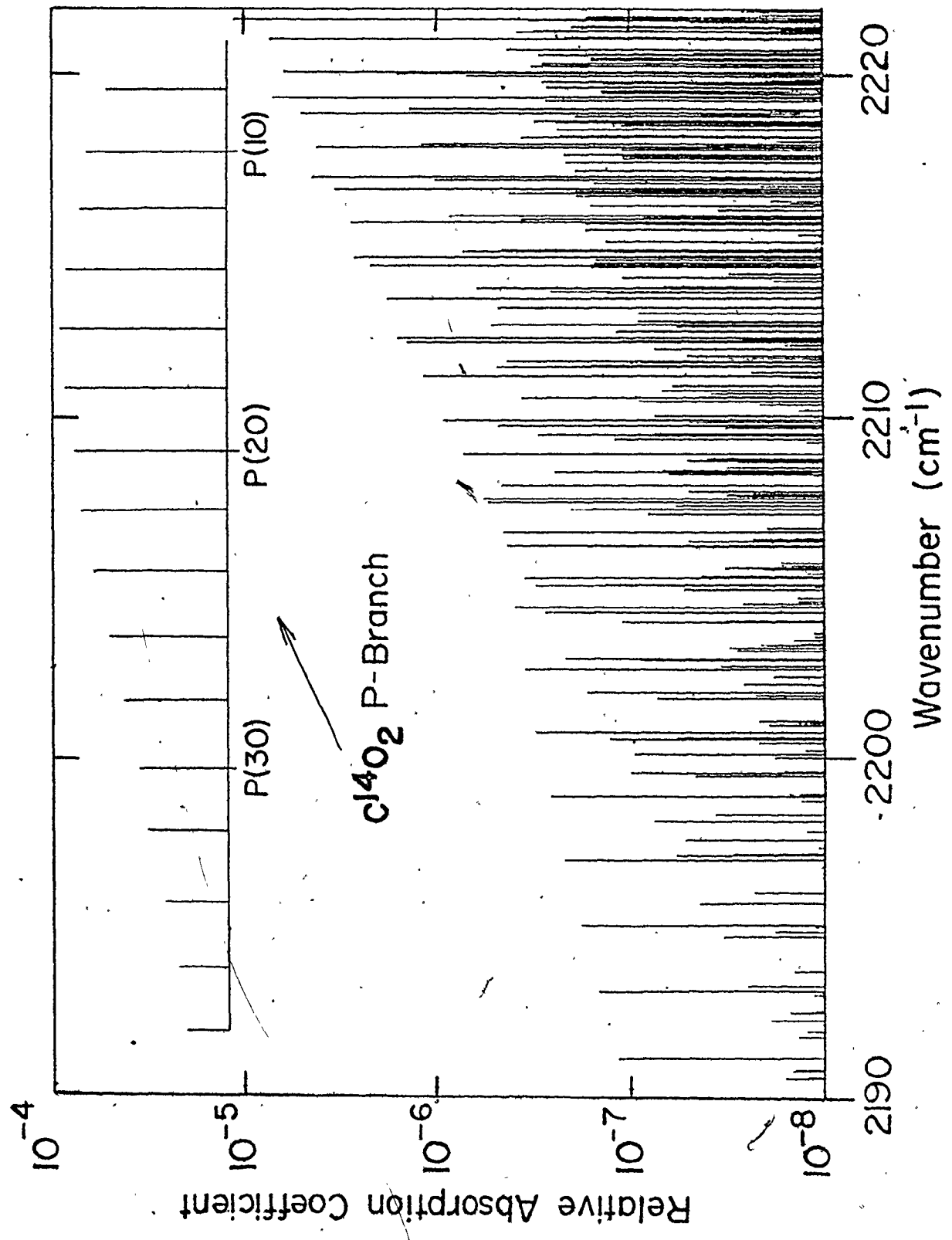


isotopic abundance relative to  $C^{12}O^{16}_2$ . Each band of each isotope has a P and an R branch, which are clearly shown on the  $C^{14}O^{16}_2$  band. The individual lines in the bands are plotted in a linear fashion to preserve the usual P and R-branch structure. Despite the large isotope shift between the  $\nu_3$  bands of  $^{14}CO_2$  ( $2226\text{ cm}^{-1}$ ) and  $C^{12}O^{16}_2$  ( $2349\text{ cm}^{-1}$ ), there are still many overlapping lines, particularly in the R-branch of  $C^{14}O_2$ . Most of these overlapping lines are caused by the heavier isotopic species of  $CO_2$  (i.e.,  $C^{13}O^{18}_2$ ), which have  $\nu_3$  bands which are shifted to smaller wavenumber. Clearly, the P-branch lines of  $C^{14}O_2$  are the best candidates for reduced interference, and we have limited our investigation to these lines.

Unfortunately, the spectra shown in Fig. 4-1 do not take into account all the hot bands (such as  $01^10-01^11$ ) which are present in  $CO_2$ . These hot bands are also shifted to longer wavelengths due to the anharmonicity of the molecule. Figure 4-2 shows a more complete spectra of  $CO_2$  in the region of the P-branch of  $C^{14}O_2$ . All line intensities are plotted on a logarithmic scale relative to the strong lines of  $C^{12}O_2$ . Only lines with intensities greater than  $10^4$  times the intensity of  $C^{14}O_2$  lines in modern samples of  $CO_2$  are included. Note that the high-J transitions in  $C^{14}O_2$  are less likely to suffer strong interferences in normal  $CO_2$ . We have attempted to include in our calculations all  $CO_2$  absorption lines which have intensities sufficient to cause

Fig. 4-2

Detailed CO<sub>2</sub> spectrum, including hot bands, in the region of the P-branch of C<sup>14</sup>O<sub>2</sub>. All lines are normalised to the strong lines in the fundamental of C<sup>12</sup>O<sup>16</sup><sub>2</sub>. Further details are given in the text.



interference in radiocarbon dating experiments. However, this requires an accurate knowledge of band constants for hot bands (lower level energies greater than  $3000 \text{ cm}^{-1}$ ) and rare isotope bands (such as  $\text{O}^{17}\text{C}^{13}\text{O}^{18}$ ). This data is not available, and in its place we have carried out experimental measurements using the tunable diode laser. Our aim is to find a  $\text{C}^{14}\text{O}_2$  line which has little or no interference from absorption lines in normal  $\text{CO}_2$ .

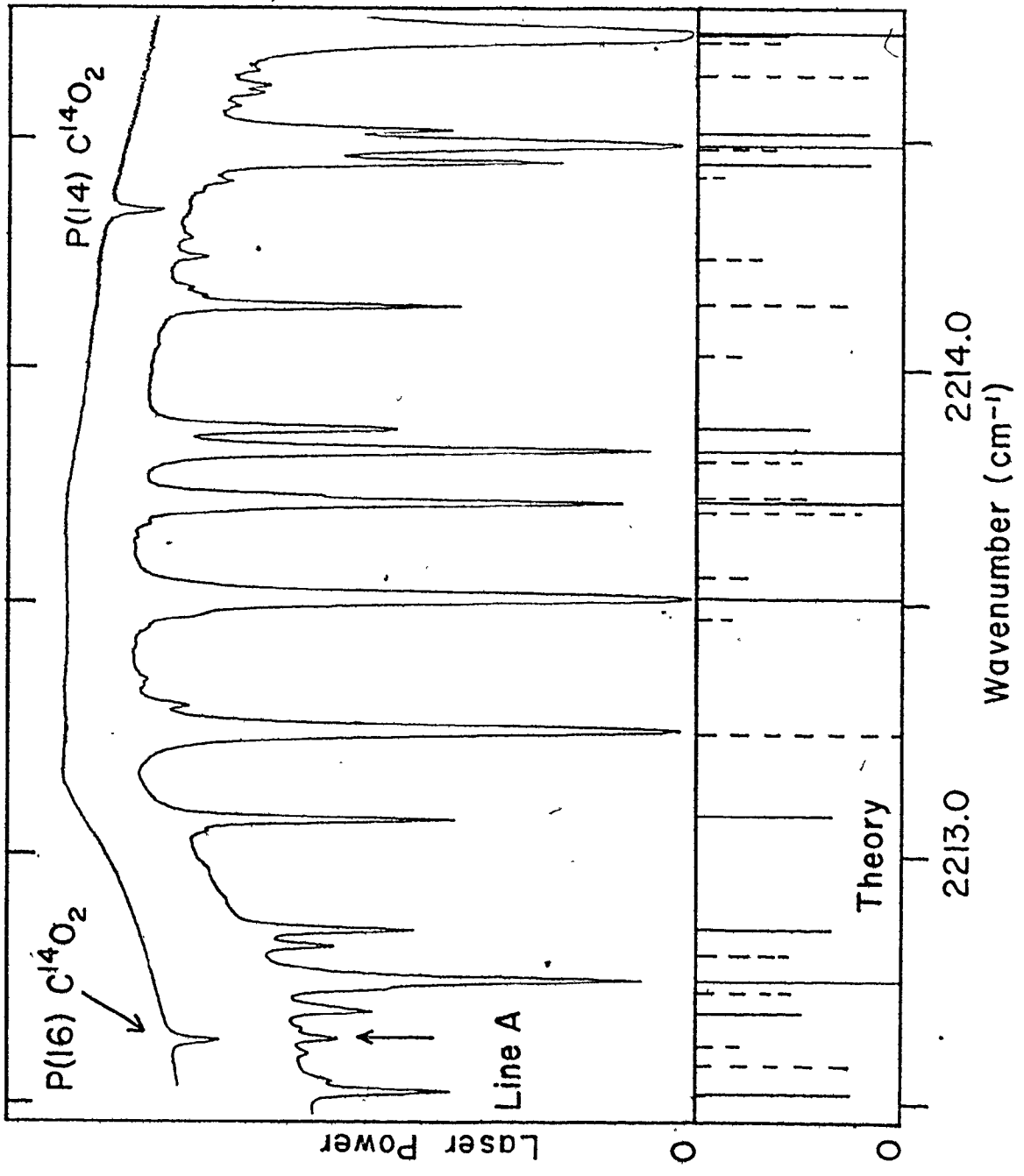
#### 4) 3 Line-by-Line Evaluation of the P-Branch of $\text{C}^{14}\text{O}_2$

The apparatus described in the second chapter is used to carry out a systematic search on all the strong P branch lines of  $\text{C}^{14}\text{O}_2$  to determine which lines are relatively free from interference. Figure 4-3 shows a typical absorption spectrum taken under direct detection in the spectral region of the P(16) and P(14)  $\text{C}^{14}\text{O}_2$  lines. This trace was obtained by passing the laser beam through a 200 m pathlength of  $\text{CO}_2$  at a pressure of 30 Torr. An absorption spectrum in pure  $\text{N}_2\text{O}$  was also recorded. The  $\text{N}_2\text{O}$  spectrum was used to calibrate the laser wavelength as a function of the diode current. ( $\text{N}_2\text{O}$  is chosen for this purpose as the  $\text{N}_2\text{O}$  spectrum has recently been measured with very high accuracy [22]-[24].) Using this calibration, an accurate comparison can be made between the observed absorption spectrum and the calculated spectrum shown at the bottom of the trace. Line positions indicated by (—) are taken from [10]-[16] with typical errors of  $\pm 0.005 \text{ cm}^{-1}$ . These lines show a good agreement with the mea-

Fig. 4-3

Results of diode scans over the P(16) and P(14) lines of  $C^{14}O_2$ . The lower trace was taken with a pathlength of 200 m through  $CO_2$  at a pressure of 30 Torr. For the upper trace the multipass cell was evacuated, and a small cell of  $C^{14}O_2$  inserted in the laser beam. Note that the P(16) line is overlapped by line A, while the P(14) line is relatively free from interference. The theoretical absorption spectrum is calculated using the linestrengths of [17]. Line positions indicated by (—) are taken from [10]-[16], while those indicated by (---) are from the less accurate AFGL compilation [17], [18]. Experimental line positions were determined by calibrating the diode tuning rate using a  $N_2O$  reference cell [22]-[24].





7

sured spectrum. The calculated lines indicated by (---) are taken from the AFGL compilation [17], [18]. In general, this compilation is much less accurate, as can be seen by comparison with the experimental spectrum. The upper trace in Fig. 4-3 was taken with the multipass cell evacuated and a small cell of  $C^{14}O_2$  inserted into the laser beam. Note that the P(16) line is overlapped by line A, while the P(14) line is relatively free from interference. Line A has an absorption coefficient at 30 Torr of  $\sim 5 \times 10^{-4} \text{ m}^{-1}$ . This strong interfering line renders the P(16) line useless for radiocarbon dating. The small dip coincident with the P(14) line is a weak doublet which can be resolved at lower pressure ( $\sim 10$  Torr). Figure 4-4 shows an absorption spectrum taken under identical conditions near the P(38) line of  $C^{14}O_2$ . Note the reduction in the number of strong absorption lines as the spectral region shifts to longer wavelength. Second harmonic detection, fully described in chapter 3, is employed to record the lower traces. Expanded views of the P(38) region are shown in Fig. 4-5. From Fig. 4-5, we determine that an interfering line is exactly coincident with the P(38) line and has an absorption coefficient of  $3.8 \times 10^{-6} \text{ m}^{-1}$  at 30 Torr. We investigated all  $C^{14}O_2$  lines between P(12) and P(38). The results of the line-by-line investigation are summarized in Table 4-1.

The results shown in Table 4-1 might lead one to identify the P(38)  $C^{14}O_2$  line as the most suitable for radiocarbon detection. However, at room temperature the P(38)

Fig. 4-4

Diode scans taken near P(38) line of  $C^{14}O_2$  through 200 m pathlength at a pressure of 30 Torr. The upper and lower traces were taken with direct and 2f. detection respectively. Two diode traces shown in Fig. 4-4 were recorded with a 10 cm cell of  $C^{14}O_2$  placed in the laser beam.

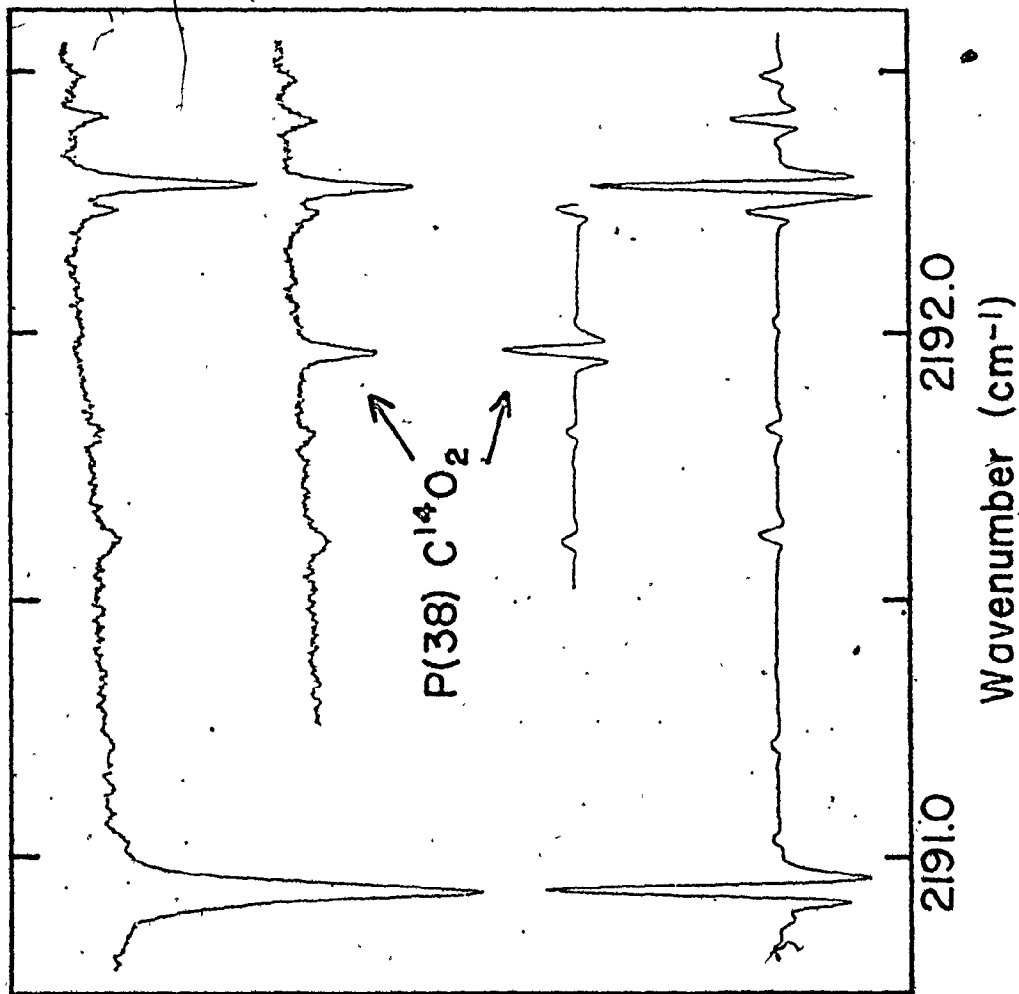


Fig. 4-5

More sensitive scans of the region around the P(38)  $C^{14}O_2$  line. The arrow below the lowest trace indicates the position of the P(38)  $C^{14}O_2$  line. The upper trace is an expanded view of the interfering line which has an intensity equivalent to the intensity of P(38) line with a  $C^{14}O_2$  concentration of  $\sim 1$  ppb.

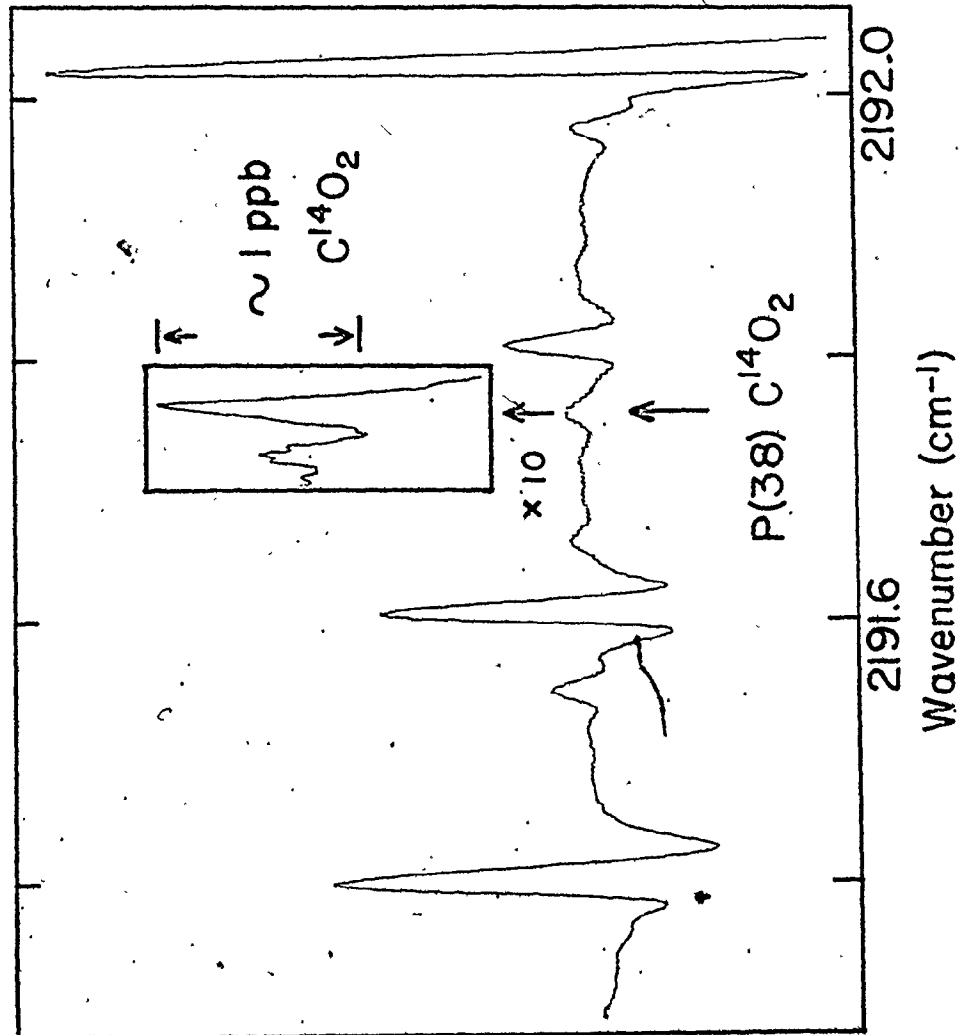


Table 4-1

List of lines in normal CO<sub>2</sub> which overlap and interfere with C<sup>14</sup>O<sub>2</sub> P-branch lines.

C <sup>14</sup> O <sub>2</sub> line P(J)	Absorption coefficient of interfering line at room temperature (a) m <sup>-1</sup>	Line Separation C <sup>14</sup> O <sub>2</sub> line - interference (b) MHz
12 (c)	5.5 × 10 <sup>-5</sup>	330
14 (c)	2.9 × 10 <sup>-5</sup>	120
16	6.1 × 10 <sup>-4</sup>	80
18	3.3 × 10 <sup>-4</sup>	-270
20 (c)	3.8 × 10 <sup>-5</sup>	-250
22	6.9 × 10 <sup>-3</sup>	-300
24	2.8 × 10 <sup>-4</sup>	- 50
26	4.3 × 10 <sup>-4</sup>	480
28 (c)	2.7 × 10 <sup>-5</sup>	-140
30	2.6 × 10 <sup>-3</sup>	-420
32	1.9 × 10 <sup>-5</sup>	180
34	1.0 × 10 <sup>-4</sup>	360
36	1.2 × 10 <sup>-4</sup>	210
38	4.6 × 10 <sup>-6</sup>	0

(a) All absorption coefficients have an accuracy of ± 15% and are given for a CO<sub>2</sub> pressure of 50 Torr (pressure broadened regime).

(b) Typical accuracy on separation measurement is ± 30 MHz.

(c) Lines selected for further study. The P(32) and P(38) lines were not given further consideration, as their line-strengths are weak relative to P(20) (see Fig. 4-2).

linestrength is only one quarter of the strength of the strongest  $C^{14}O_2$  lines. (If the gas is cooled, the relative P(38) linestrength becomes even smaller). Hence, although the P(38) line is the most favorable as far as interference is concerned, it is a poor choice from the point of view of sensitivity. A similar problem occurs for the P(32) line. Consequently, we have chosen to concentrate on the P(12), P(14), P(20) and P(28) lines. These four  $^{14}CO_2$  lines combine maximum linestrength with small background interference. Initially, we chose P(20) for further study. The diode laser was tuned to operate in single mode in the wavelength region around P(20) of  $C^{14}O_2$ , and the spectrometer was removed. For convenience we replaced the 5 m multipass cell with a 1 m cell [25], and aligned the optics to minimize optical fringes and optimize sensitivity [26]. Figure 4-6 shows two diode traces taken with, and without, the  $C^{14}O_2$  reference cell in the beam. From the lower trace taken with 2f detection, the background near P(20) line appears almost flat. Expanded views of the region around the P(20) line are shown in Fig. 4-7. Also shown in Fig. 4-7 is a line representing the P(20) line of  $C^{14}O_2$  at a concentration of 1.6 ppb  $C^{14}O_2$ . Clearly, line B interferes with the  $C^{14}O_2$  P(20) line, and has a strength equivalent to 2.2 ppb  $C^{14}O_2$  or 1700 times modern abundance. Even taking into account the frequency separation between the two lines, line B contributes a signal equivalent to 770 times modern abundance at the P(20) line centre. As



<  
Fig. 4-6

Diode laser scans of the wavenumber region near the P(20) line of  $C^{14}O_2$ . The upper trace is taken using direct detection. The laser beam passes through a 32 m path-length of normal  $CO_2$  at 20 Torr, followed by a small cell containing  $C^{14}O_2$ . For the lower trace the  $C^{14}O_2$  cell is removed, and second harmonic is employed.

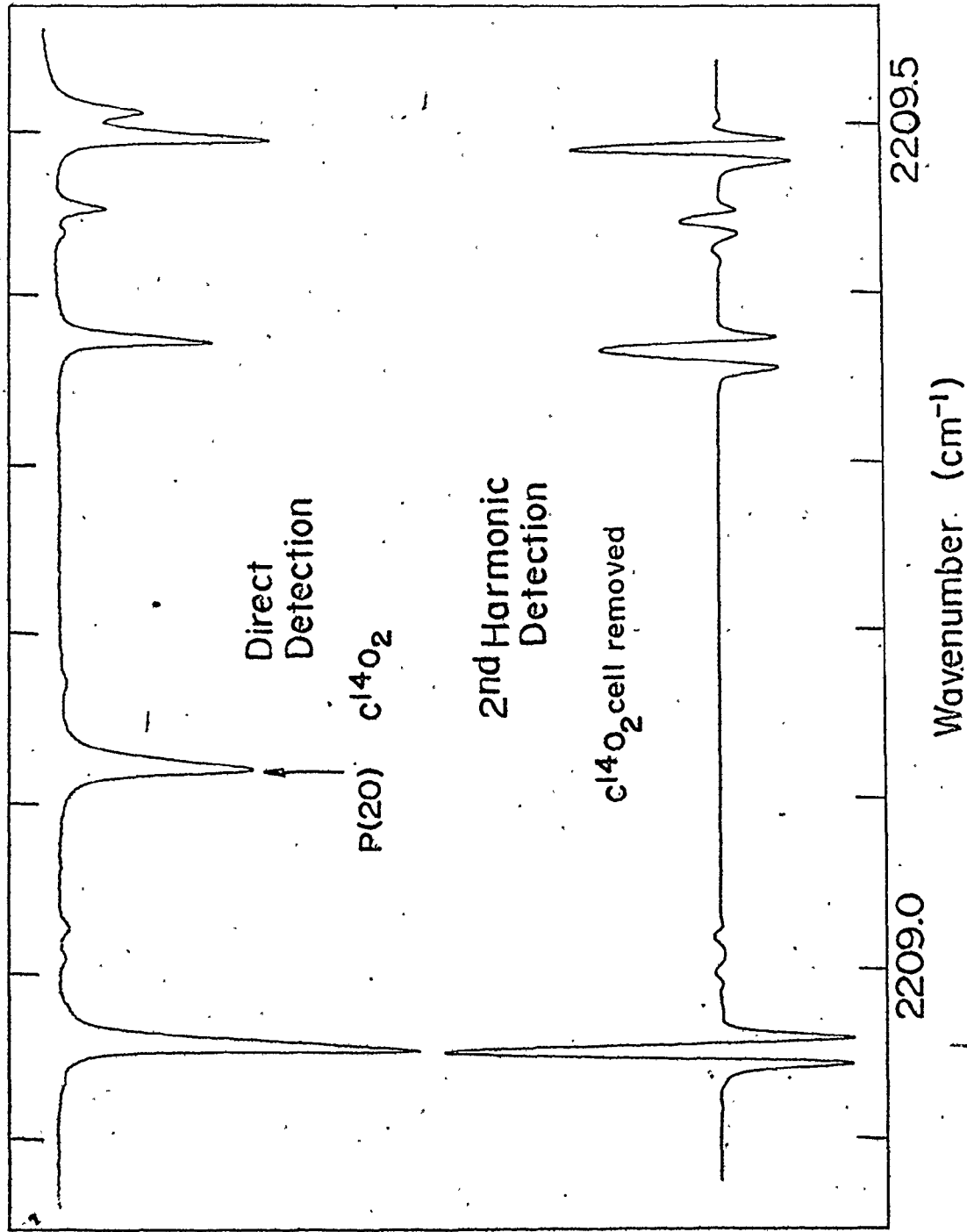
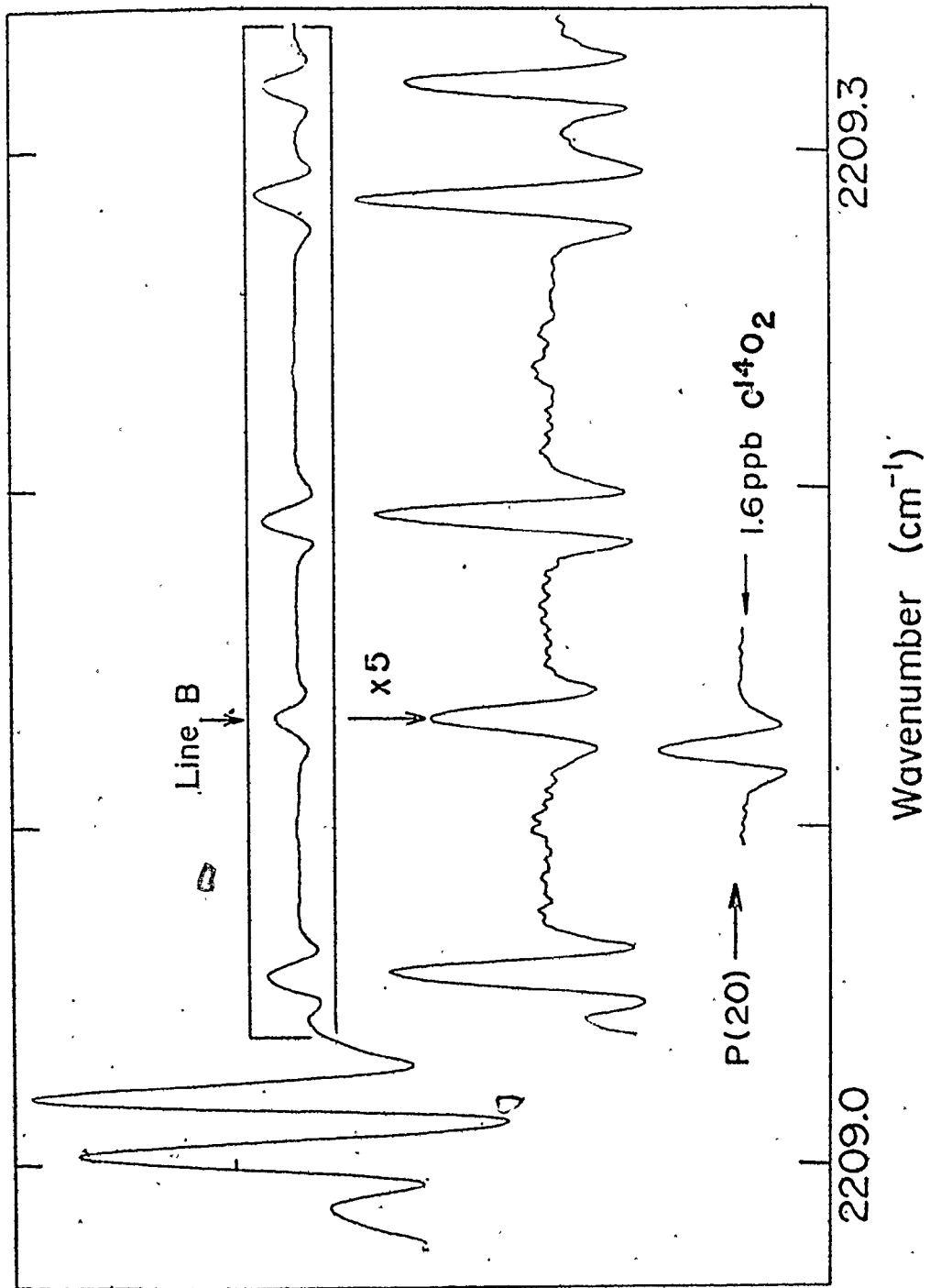


Fig. 4-7

More sensitive scans of the region around the P(20)  $C^{14}O_2$  line. The weak line B is present in normal  $CO_2$  and overlaps the P(20)  $C^{14}O_2$  line which is represented by the trace at the bottom of the Figure. The displayed P(20) line is equivalent to a  $C^{14}O_2$  concentration of 1.6 ppb, and the offset from line B is 250 MHz.



can be seen from Table 4-1, a similar or greater level of interference occurs for all the strong  $C^{14}O_2$  lines. This poses a severe problem for radiocarbon dating, unless steps are taken to suppress the interference.

#### 4.4 Summary

This chapter gives a description of the absorption spectrum of  $CO_2$  in the spectral region of the P-branch of the  $\nu_3$  band of  $C^{14}O_2$ . Experimental results on the detection limits of  $C^{14}O_2$  in normal  $CO_2$  at room temperature are presented. We identified the four most favorable spectral regions for radiocarbon dating. The main limitation on the detection of  $C^{14}O_2$  in room temperature  $CO_2$  is shown to be the background of interfering lines. Details of an effective technique for eliminating this interference problem are given in the next chapter.

## CHAPTER 5

ELIMINATION OF INTERFERING BACKGROUND LINES IN CO<sub>2</sub>5.1 Introduction

In the last chapter it is shown that the main limitation to the detection of C<sup>14</sup> in room temperature gas samples is the background of interfering lines. These detection limits can be improved by using a background subtraction technique. If we employ a sample of carbon with no C<sup>14</sup> (eg., coal) the background of interfering lines in CO<sub>2</sub> can be obtained. This background spectrum can then be subtracted from a spectrum taken in modern CO<sub>2</sub> to determine the absorption coefficient associated with the C<sup>14</sup>O<sub>2</sub> lines. Normalization of the two spectra is easily carried out by using lines well separated from the C<sup>14</sup>O<sub>2</sub> lines. Preliminary investigations of this technique indicate a reduction in background interference by a factor of 100 can be attained. However, even this improvement in sensitivity is still insufficient for radiocarbon dating.

Fortunately, the interference line strength shown in Table 4-1 only holds at room temperature. All the weak interfering lines are expected to be hot band lines, with lower levels lying high above the ground state. Hence cooling the gas sample to dry ice temperature should greatly reduce the

linestrength of the interferences relative to the  $C^{14}O_2$  lines. To estimate this reduction in the intensity of the interfering lines, one must know the energy of their lower levels, ( $E_L$ ). As the interfering lines could not be identified from available spectroscopic data a direct experimental determination was made, as described in the next section.

## 5.2 Measurement of the Lower Level Energy of Interfering Lines

To obtain maximum accuracy on the determination of  $E_L$  for the interfering lines we chose to heat the  $CO_2$  gas and measure the increase in absorption coefficient. (If one attempts to measure  $E_L$  by cooling the gas, the weak lines under investigation tend to reduce in intensity by several orders of magnitude, and consequently vanish below the system noise level). The configuration used to make these measurements is shown in Fig. 5-1. The laser output is collected by a 5 cm focal length lens and focused into a single pass 1 m cell of hot  $CO_2$  [27]. The output beam from the cell is directly focused onto a HgCdTe detector. Flow rate and pressure inside the cell were well controlled giving a long term stability of  $\pm 4\%$  on the absorption measurements:

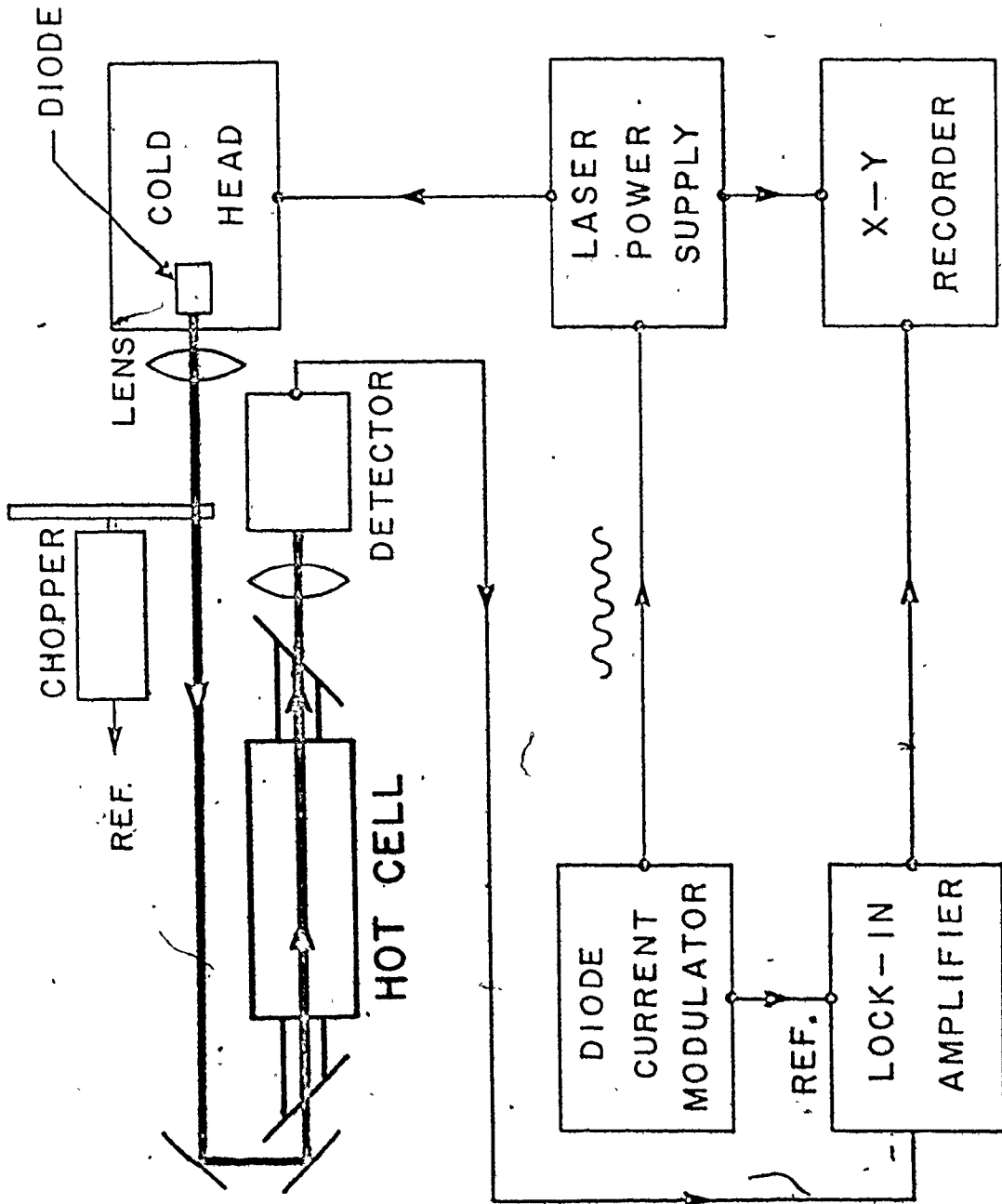
When the gas is heated, the absorption coefficient of a line changes according to Equ. 5-1 below:

$$\frac{\alpha_H}{\alpha_R} = \frac{Q_V(T_R)}{Q_V(T_H)} \times \left(\frac{T_R}{T_H}\right)^{5/2} \times \exp[E_L \times \left(\frac{1}{T_R} - \frac{1}{T_H}\right)] \times \frac{V(O, a(P_H, T_H))}{V(O, a(P_R, T_R))} \quad (5-1)$$

Fig. 5-1

Schematic diagram of the apparatus used to determine the lower energy level of the interfering lines.





where  $Q_V(T_i)$  is the vibrational partition function at temperature  $T_i$ ,  $\alpha_H$  and  $\alpha_R$  are the absorption coefficients at temperatures  $T_H$  and  $T_R$  respectively,  $E_L$  is the lower energy level in units of K,  $V(0, a(P_i, T_i))$  is the Voigt function evaluated at line centre,  $a(P_i, T_i) = \frac{\Delta v_L(P_i, T_i)}{\Delta v_D(T_i)} \times (\ln 2)^{1/2}$ , and  $T_H$ ,  $T_R$  are the hot and room temperature respectively. The temperature of the hot  $\text{CO}_2$  was chosen to obtain a substantial change in absorption of the interfering lines, while minimising the number of additional lines which appeared in the spectrum. Optimum temperature was found to be  $\approx 370$  K.

The gas pressure was chosen such that the Voigt contribution to the ratio is nearly the same for all lines. Under those experimental conditions, we can rewrite equation (5-1) as:

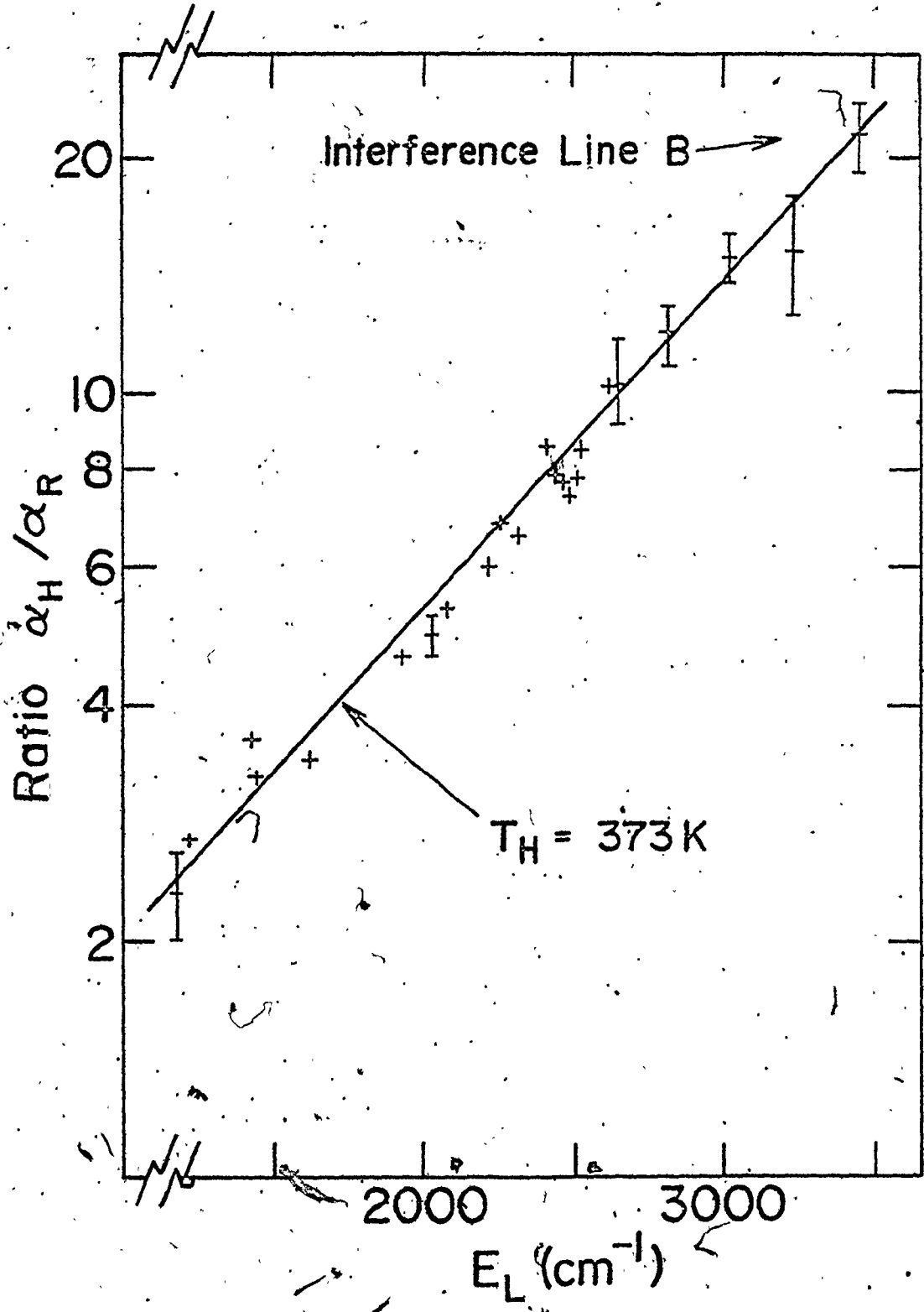
$$\frac{\alpha_H}{\alpha_R} = C \exp[E_L \times (\frac{1}{T_R} - \frac{1}{T_H})] \quad (5-2)$$

where the constant  $C$  is the same for all lines. Hence, by comparing the measured ratio  $\alpha_H/\alpha_R$  for lines of known  $E_L$  with  $\alpha_H/\alpha_R$  for unknown lines, we can determine the lower energy level. We have chosen several known lines in different spectral regions to ensure a wide range of  $E_L$  values.

Figure 5-2 shows a semilog plot of the ratio  $\alpha_H/\alpha_R$  as a function of  $E_L$  for the known lines. Also shown is the measured ratio for line B (see Fig. 4-7) and typical error bars. A straight line is drawn through the data points by using a least-squares fit. From the slope of the line, we

Fig. 5-2

Plot of  $\ln(\alpha_H/\alpha_R)$  as a function of lower energy level in  $\text{cm}^{-1}$  ( $E_L$ ) for several  $\text{CO}_2$  absorption lines. Only those lines which have been unambiguously identified are used in these measurements. Typical error bars are shown, and the straight line through the data points is derived from Equation 5-2 with  $T_H = 373$  K. The measured value of  $\alpha_H/\alpha_R$  for line B of Fig. 4-7 is also shown.



determine the effective temperature [28] in the heated gas as  $373 \pm 3$  K. The results shown in Fig. 5-2 enable us to estimate  $E_L$  for line B as  $3430 \pm 140$   $\text{cm}^{-1}$ . Similar measurements of  $E_L$  were made for the  $\text{CO}_2$  lines interfering with the P(12), P(14) and P(28) line of  $\text{C}^{14}\text{O}_2$ . This information allows us to estimate the improvement to be attained upon cooling the gas.

Table 5-1 summarizes the effect of cooling in  $\text{CO}_2$  for the most promising  $\text{C}^{14}\text{O}_2$  lines. Cooling alone, or cooling plus the use of the background subtraction technique mentioned earlier, can be used to remove the interfering lines in a sample of  $\text{CO}_2$ . The most suitable line is the P(20) line of  $\text{C}^{14}\text{O}_2$ . P(14) and P(28) are alternative possible candidates. Other lines listed in Table 4-1 may also be suitable for dating purposes, provided the interfering lines have a sufficiently large value of  $E_L$ .

### 5.3 Cooling Effects on the Absorption Spectrum

In order to verify the effects of cooling on the absorption spectrum, an experiment was carried out with the gas at dry ice temperature. We observed that most of the  $\text{CO}_2$  lines present at room temperature vanished upon cooling. The only lines appearing above the noise level either belonged to  $\text{CO}_2$  transitions with small values of  $E_L$ , or were contaminant lines of  $\text{N}_2\text{O}$  and  $\text{CO}$ .

In this experiment, we replaced the single pass 1 m cell of hot  $\text{CO}_2$  in the configuration described in section 5.2 by a 1 m cell of  $\text{CO}_2$  cooled in dry ice. Figure 5-3 shows a

Table 5-1

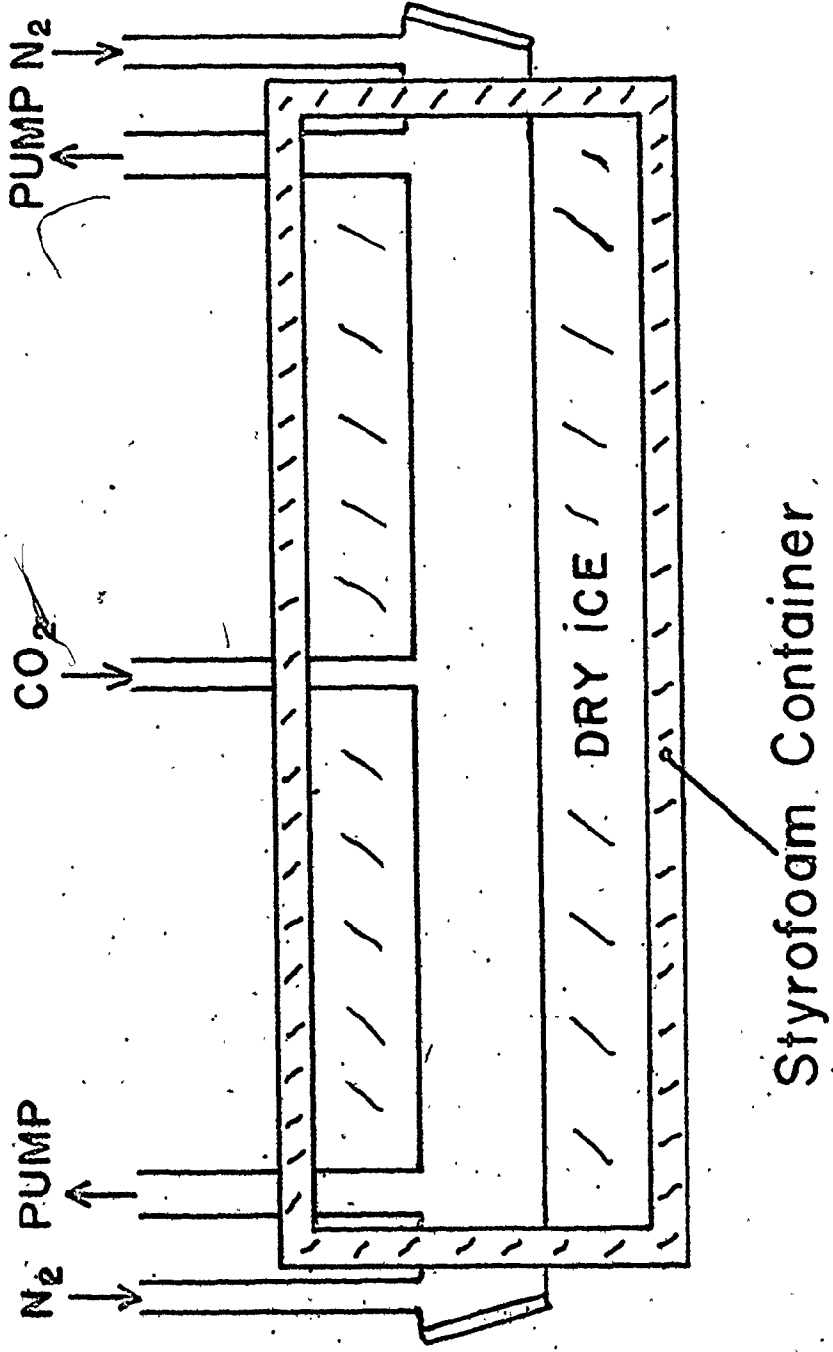
Calculated reduction in interference on cooling the CO<sub>2</sub> sample

C <sup>14</sup> O <sub>2</sub> Line	E <sub>L</sub> for Inter- fering Line cm <sup>-1</sup>	Interference factor at C <sup>14</sup> O <sub>2</sub> linecentre (a) T = 298 K	Interference factor T = 195 K (b) (dry ice)	Interference factor T = 170 K (b)
P(12)	2170	950	4.4	0.44
P(14)	3320	910	0.24	7.0 × 10 <sup>-3</sup>
P(20)	3430	770	0.19	5.4 × 10 <sup>-3</sup>
P(28)	3480	1000	0.31	9.9 × 10 <sup>-3</sup>

- (a) Interference factor is defined in relative units normalized to the absorption produced by the C<sup>14</sup>O<sub>2</sub> present in a modern sample. The interference and C<sup>14</sup>O<sub>2</sub> signals are evaluated at C<sup>14</sup>O<sub>2</sub> linecentre.
- (b) The pressure used at low temperature is determined from the condition that the lineshape contribution to the absorption coefficient has to be the same at both low and room temperatures. For instance, the lineshape contribution at T = 298 K and at a pressure of 20 Torr is equal to that at T = 195 K and at a pressure of 14 Torr.

Fig. 5-3

Schematic diagram of the 1 m cold cell.



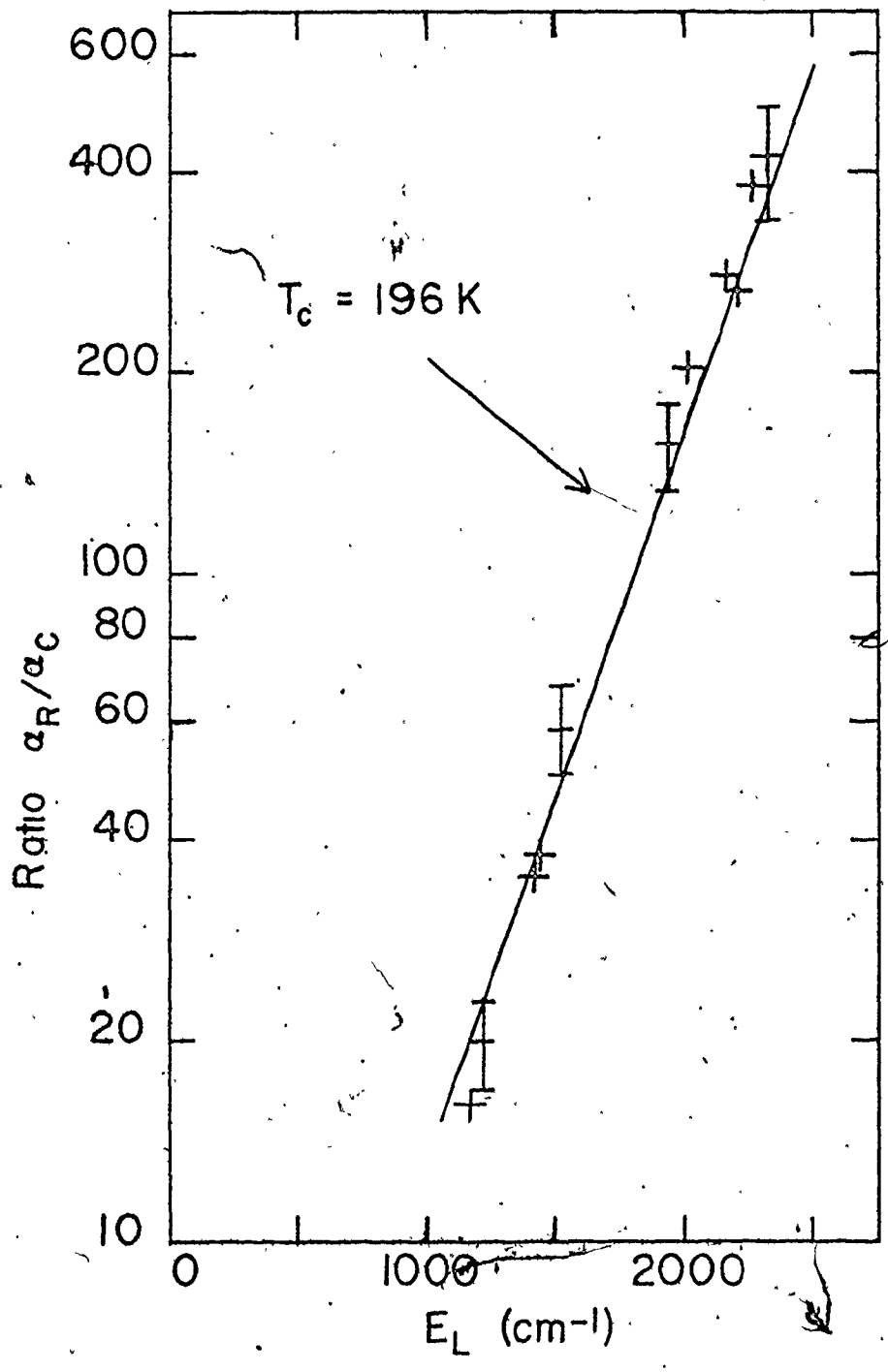


schematic of the 1 m cold cell. The cell is enclosed in a styrofoam box which contains dry ice.  $N_2$  is used as a buffer gas to prevent any hot region of  $CO_2$  gas near the windows. Once the gas was cooled to dry ice temperature, several traces were taken in the same spectral regions as those described in section 5.2.

Most of the  $CO_2$  lines seen in the room temperature scans became so weak at dry ice temperature that they could not be detected with the available sensitivity ( $\sim 7 \times 10^{-6} \text{ m}^{-1}$  in a 1 m pathlength). Only a few  $CO_2$  lines could be observed at dry ice temperature, and these were easily identified as having relatively low values of  $E_L$ . Once again we compared absorption coefficients at room temperature ( $\alpha_R$ ) with those observed in the cooled cell ( $\alpha_C$ ). This enabled us to confirm that the reduction in intensity of all lines on cooling followed the expected behavior. Figure 5-4 shows a semilog plot of the ratio  $\alpha_R/\alpha_C$  as a function of  $E_L$ . The measurements of the absorption coefficient at low temperature were obtained by using 2f detection. The minimum detectable absorption coefficient that can be measured with a time constant of 0.3 sec and with a SNR of 1 is  $\sim 7 \times 10^{-6} \text{ m}^{-1}$ . Also shown in Fig. 5-4 is a straight line which was fitted to the data points. From the slope of the line, the gas temperature was determined to be 196 K, in excellent agreement with the temperature of dry ice 196.5 K.

Fig. 5-4

Plot of  $\ln(\alpha_R/\alpha_C)$  as a function of the lower energy level in  $\text{cm}^{-1}$  ( $E_L$ ) for several  $\text{CO}_2$  absorption lines. Only the lines with known  $E_L$  appearing above the noise level were selected. A straight line is fitted through the data points with  $T_C = 196$  K.



The data taken in the cooled  $\text{CO}_2$  cell was not expected to furnish any information on the weak interfering lines listed in Table 4-1 as they are so much reduced in intensity as to vanish below the noise level. However, the experiments with cooled  $\text{CO}_2$  did enable us to confirm the expected reduction in intensity on cooling, and to ensure that no unexpected contaminants were present.

#### 5.4 Summary

By comparing the increase in absorption coefficient of the interfering lines in warm  $\text{CO}_2$  with the increase of known lines, a determination of the lower energy level of the interfering lines is achieved. Consequently, the effect of cooling on the interfering lines can be estimated, showing that the background of interfering lines is no longer a problem. The effect of cooling is also verified experimentally with the use of known absorption lines. Thus from these results, we are confident that the detection of  $\text{C}^{14}\text{O}_2$  in a cooled multipass cell will not be limited by interferences from the stable isotopic forms of  $\text{CO}_2$ . The next chapter treats the problem of achieving sufficient sensitivity to do practical radio-carbon dating.

## CHAPTER 6

### NOISE CHARACTERISTICS AND SENSITIVITY LIMITS OF THE LASER ABSORPTION SPECTROMETER

#### 6.1 Introduction

In order to determine the required sensitivity for practical radiocarbon dating one must know the linestrength of the  $\nu_3$  fundamental band of  $C^{14}O_2$  and the concentration of  $C^{14}$  atoms in a modern sample of carbon. The linestrengths of the strong  $C^{14}O_2$  lines have been measured by Whalen et al. [21]. If one combines their results with the concentration of  $C^{14}$  in a modern sample of carbon ( $C^{14}/C^{12} \sim 1.3 \times 10^{-12}$ , [29]), the absorption coefficient of the P(20)  $C^{14}O_2$  line at a temperature of 195 K and at  $\sim 14$  Torr total pressure is  $2.2 \times 10^{-8} \text{ m}^{-1}$ . Thus, any practical radiocarbon dating apparatus should have an equivalent noise level of  $\leq 2 \times 10^{-9} \text{ m}^{-1}$ .

In a recent paper, Reid et al. [26] investigated the factors which limit the sensitivity of the Laser Absorption Spectrometer (LAS). Their investigations were restricted to short time constants and a small multipass cell of 1 m base pathlength. The observed noise level (for a 1 sec time constant) was equivalent to an absorption coefficient of  $2 \times 10^{-7} \text{ m}^{-1}$ , a factor of 100 less than is required for radiocarbon dating.

In this chapter a brief description is given of the techniques used in analysing the LAS sensitivity for short time constants, and we report experimental results which extend the measurements of Reid et al. to much longer time constants. These experimental results enable us to predict the effect of signal averaging upon the LAS sensitivity, and to recommend procedures which may produce the required factor of 100 increase in sensitivity.

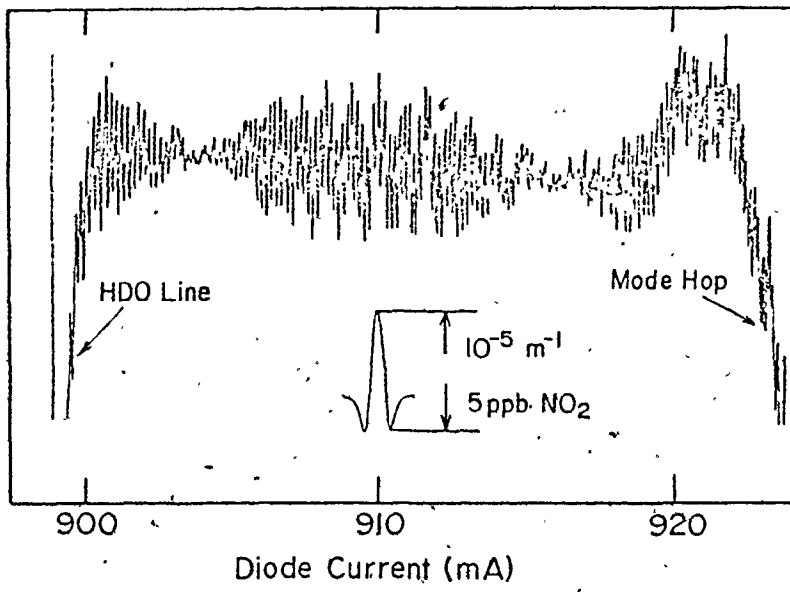
## 6.2 LAS Sensitivity with Short Time Constants

The technique used for short time constant measurements follow those developed by Reid et al. In this section we use some of the results published by Reid et al. [26] to illustrate these techniques, and to discuss the various noise mechanisms present in the LAS system.

The diode was arranged to operate in a single mode. The 1 m base pathlength multipass cell [25] was set for 40 m total pathlength and the cell was evacuated to  $< 1$  Torr. Figure 6-1 shows the  $2f$  signal of the laser power measured at the detector as a function of diode current. At high sensitivity, the tuning range of the diode laser is limited by an absorption line of HDO at 898 mA, and by the end of the single mode region (mode hop) at 924 mA. The regular oscillations seen in Fig. 6-1 are caused by optical fringes, and are typical of results obtained when the diode laser/multipass cell

Fig. 6-1

High sensitivity scan of multipass cell set for 40 m. Fringes are caused by interference between the main optical beam making 40 passes through the cell and the much weaker beams which make 36 (or 44) passes. A second harmonic lineshape corresponding to  $\sim 5$  ppb  $\text{NO}_2$  (or  $10^{-5} \text{ m}^{-1}$  absorption coefficient) is also shown to indicate sensitivity. (Figure taken from Reid et al. [26])





systems are used. The fringe amplitude typically ranges from  $10^{-4}$  to  $10^{-2}$  of the incident power and the spacing corresponds to interference between adjacent spots on the mirror located at the input/output windows of the multipass cell. As shown in Fig. 6-1, the fringe amplitude passes through a minimum at 904 mA and at 916 mA. These minima occur when the amplitude of the sinusoidal modulation is exactly an integral number of fringe spacings. The minima are produced by a variation of the tuning rate with current while using a fixed external modulation to scan the spectral region. They can be shifted such that one minimum lies at the exact position of an absorption line. The shift is obtained by a variation of a few percent of the sinusoidal modulation amplitude. This technique is useful if observations are made over a small range of the diode current but the exact setting of the modulation amplitude is very sensitive to small drifts in the diode tuning rate.

A more efficient technique for removing the optical fringes is to superimpose a second modulation (jitter) on the diode laser current. A symmetric saw-tooth modulation was used at a frequency of  $\sim 400$  Hz, with an amplitude much smaller than the 3 kHz sinusoidal modulation used for  $2f$  detection. The jitter amplitude was used to scan the laser wavelength over exactly one fringe. The fringes were electronically cancelled by choosing the jitter period to be much smaller

ler than the time constant of the lock-in amplifier. Figure 6-2 shows the effects of this technique on the fringes. The upper traces show expanded views of the multipass cell fringes in the region of a doublet of  $\text{NO}_2$  lines near 910 mA. The jitter peak-peak amplitude is varied from 0 to 2 fringe spacings. The maximum decrease in fringe magnitude is obtained with a jitter amplitude of 1 or 2. The lower trace of Fig. 6-2 shows another scan of the region displayed in Fig. 6-1 taken with a jitter amplitude of 1 fringe spacing. A significant improvement in sensitivity is obtained over the entire current range. The small jitter amplitude has the effect of reducing the peak-peak signal of the  $2f$  lineshape by less than 10%. This technique results in an enhancement of SNR by a factor of 10 to 100.

Two methods have been developed for continuous spectral monitoring of a gas: (a) repetitive scanning over an absorption line [30] and (b) locking the laser to absorption line centre [31]. Figure 6-3 and 6-4 display results obtained with these two techniques. For Fig. 6-3, the diode laser was set to scan repetitively over the  $\text{NO}_2$  lines near 910 mA. The scans were taken with a time constant of 0.1 sec. The 1 m cell was filled with air plus a trace of  $\text{NO}_2$  at a total pressure of 30 Torr, and sealed. The  $\text{NO}_2$  concentration decreased with a time constant of  $\sim 40$  sec.

The second method of monitoring the gas concentration is shown in the lower trace of Fig. 6-4. The laser wavelength

Fig. 6-2

Effect of additional "jitter" modulation. The LAS is set for second harmonic detection at 6 kHz, but a small jitter modulation at 370 Hz was added to the main 3 kHz sinewave. The upper traces show an expanded view of the fringes as the peak to peak jitter amplitude was varied from 0 to 2 fringe spacings. The lower trace is a repeat of Fig. 6-1, but with jitter amplitude set at 1 fringe spacing. Note the significant improvement in sensitivity as the fringes are electronically "washed out". (Figure taken from Reid et al. [26])

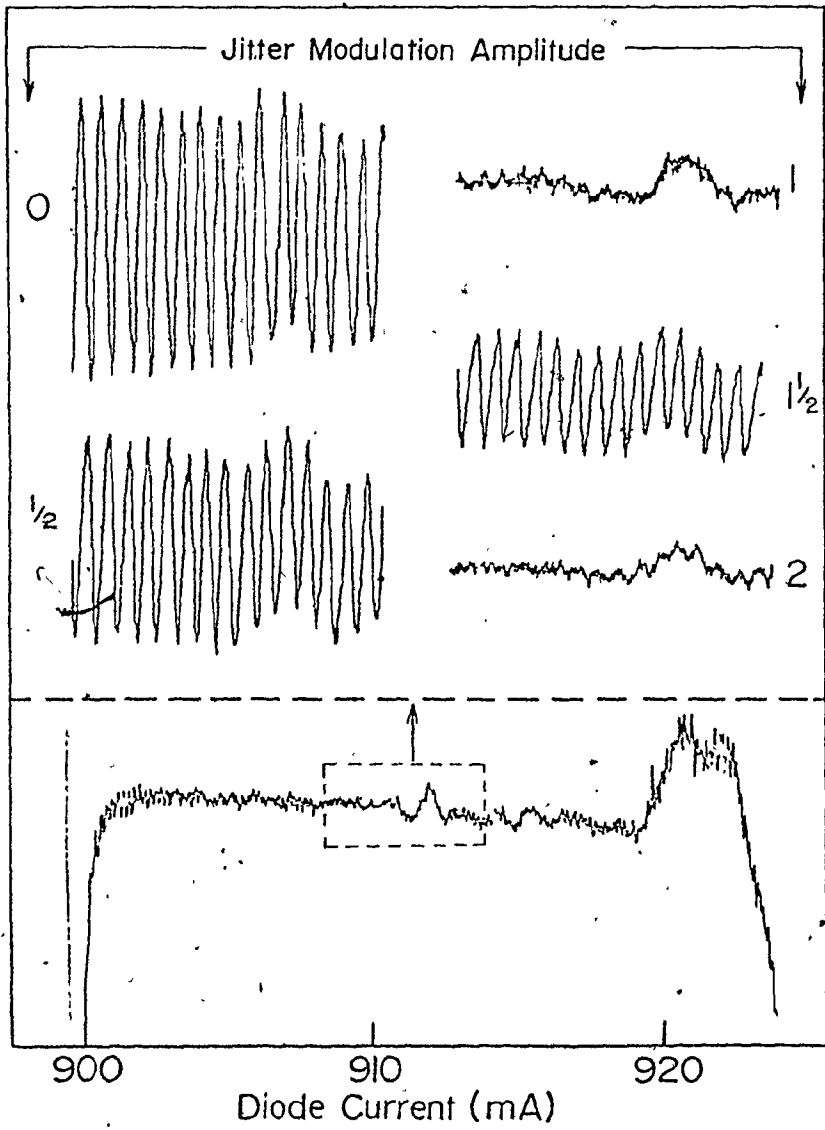


Fig. 6-3

Lifetime measurement of NO<sub>2</sub>/air mixtures in a stainless steel multipass cell. The LAS was set to scan repetitively over an NO<sub>2</sub> doublet at 1604.162, and the cell was filled with air plus a trace of NO<sub>2</sub> at ~ 30 Torr. The time constant used was only 0.1 s, but the noise level is < 1 ppb. Note the rapid decay of the NO<sub>2</sub> in the sealed cell. (Figure taken from Reid et al. [26])

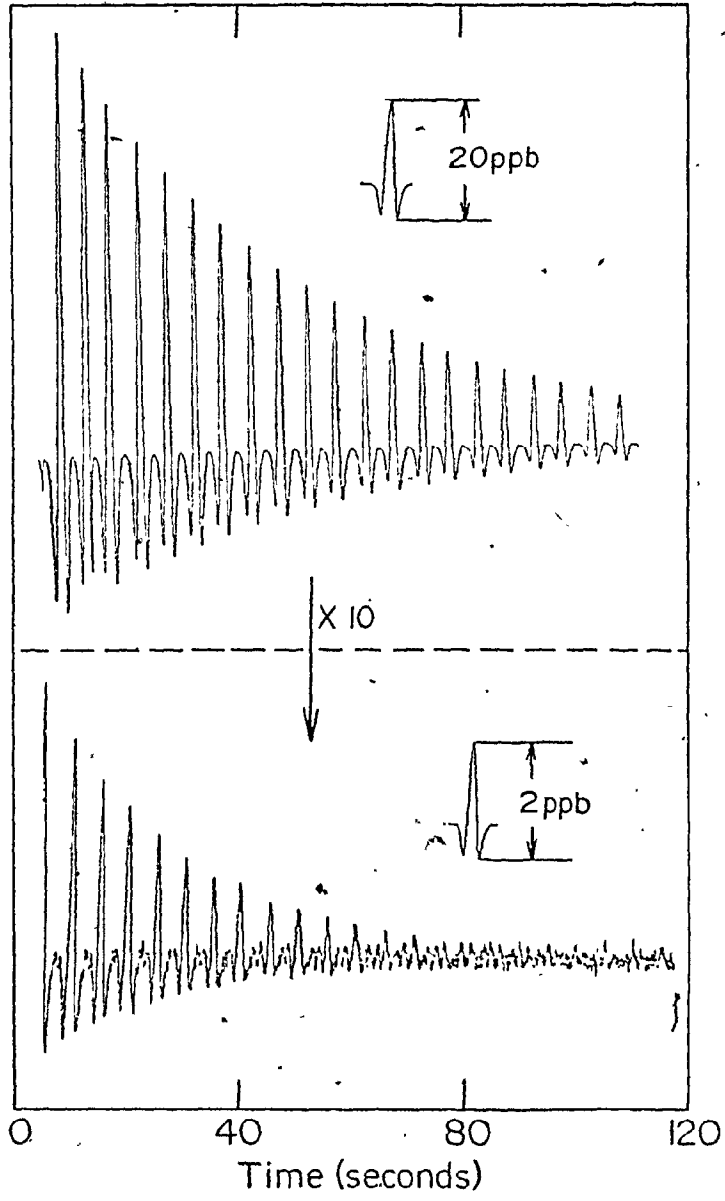
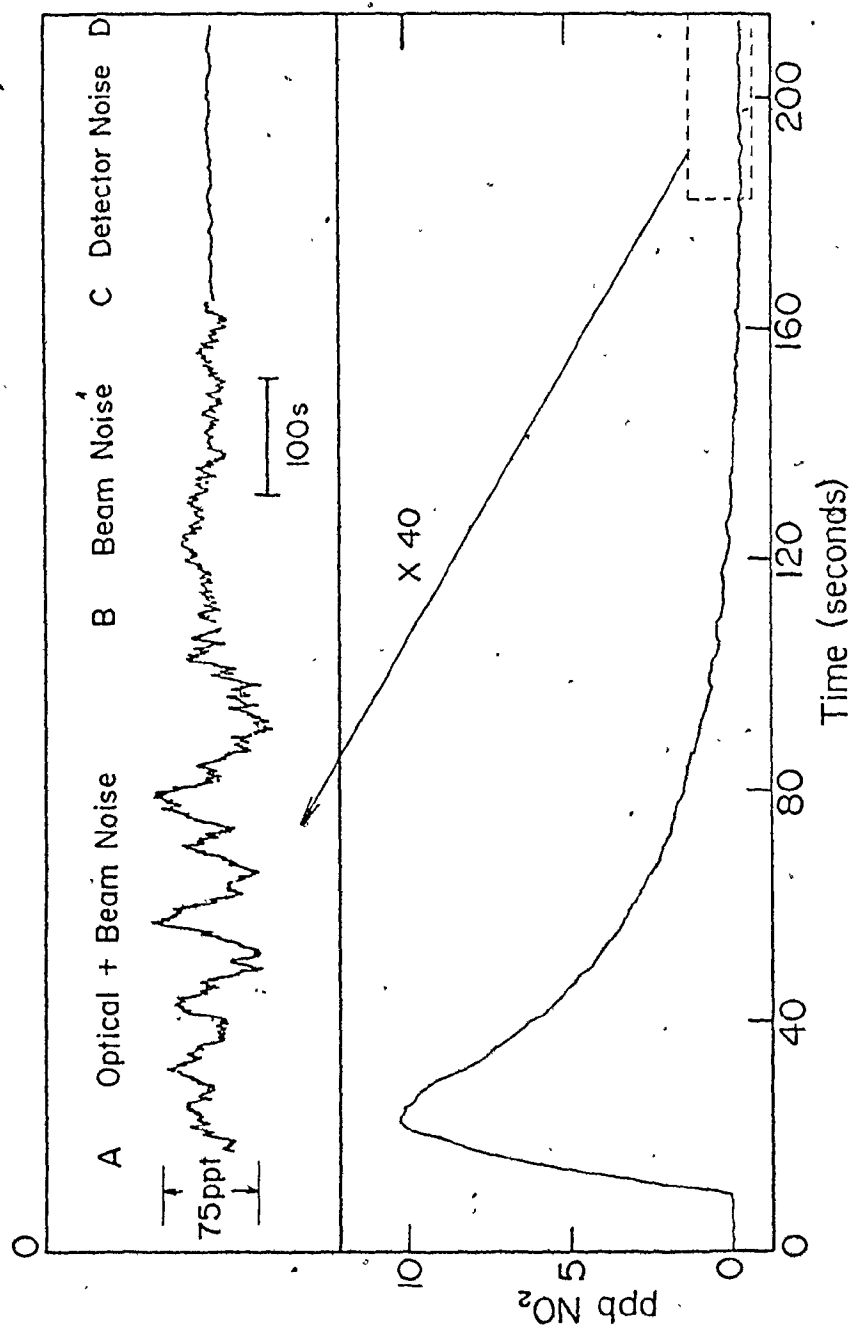


Fig. 6-4

The lower trace repeats the measurement of Fig. 6-3, but with the diode laser wavelength held at the centre of the NO<sub>2</sub> absorption line. A mixture of a few ppb NO<sub>2</sub> in air was introduced into the cell, and the concentration monitored with the LAS. The upper trace shows the noise levels which limit sensitivity. Trace A→B is an expanded view of noise under monitoring conditions, taken with a 10 s time constant. Sensitivity is 75 ppt NO<sub>2</sub> or  $1.6 \times 10^{-7} \text{ m}^{-1}$ . At time B, all modulation signals were removed from the laser current, but second harmonic detection at 6 kHz continues. Hence trace B→C records random amplitude noise on the laser beam. The final section of the trace C→D is taken with the laser switched off and corresponds to detector noise at a frequency of 6 kHz. (Figure taken from Reid et al. [26])





is locked at line centre of the  $\text{NO}_2$  doublet and any increase in  $\text{NO}_2$  concentration produces an offset voltage from the baseline [31]. At time  $t=0$ , the cell was filled with air and  $\sim 10$  ppb of  $\text{NO}_2$  was added. The LAS system measured the time evolution of the  $\text{NO}_2$  concentration with a 1 sec time constant. Expanded views of the noise levels limiting the LAS sensitivity are shown in the upper traces. The noise level obtained with a time constant of 10 sec was equivalent to an absorption coefficient of  $1.6 \times 10^{-7} \text{ m}^{-1}$ . The observed noise level is composed of the following three types of noise: detector noise, random noise and optical fringe noise. Detector noise has a negligible contribution to the total noise present in the LAS system. A more dominant noise mechanism is the laser "beam noise" which is the random power noise superposed on the laser beam [32]. The beam noise is measured when all current modulations are removed and the laser beam falls on the detector. The third type of noise, optical fringe noise, appears when the current modulations are added for trace gas detection. Because of the systematic nature of fringe noise, the ratio of optical fringe noise to beam noise varies from  $\sim 1$  to 4 when the time constant increases from 0.1 sec to 10 sec.

At present, two noise mechanisms dominate the system. The most important one is optical noise caused by multiple beams reflected in the apparatus. This is clearly a systematic type of noise and cannot be expected to average out upon

increasing the time constant of the detection system. A secondary cause of noise is the inherent amplitude noise on the laser beam. Although this noise causes problems at short time constants, it is random in nature and can be expected to reduce substantially as the system time constant is increased.

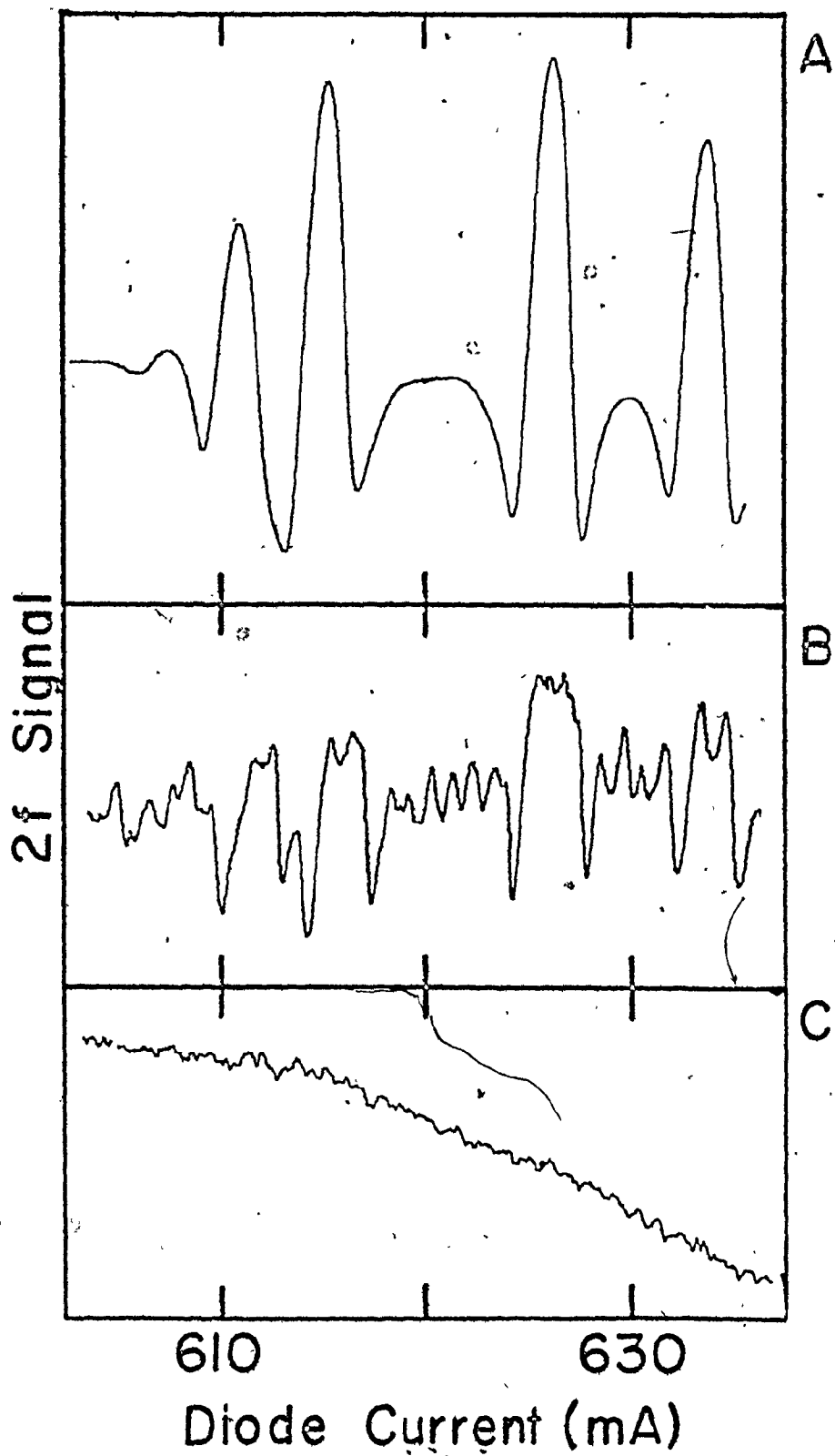
### 6.3 LAS Behavior at Long Time Constants

As conventional radiocarbon dating experiments presently take many hours per sample, we performed a series of experiments on the LAS using progressively longer time constants. Our aim was to extrapolate the results of short time constant experiment to averaging times of several hours, to determine the optimum method of signal averaging using the LAS.

The apparatus employed in this experiment was the same one used in the short time constant experiment [26]. The diode used had a ratio of random power noise (or beam noise) to total power of  $6 \times 10^{-7}$  with a 1 sec time constant (cf. Table I, [26]). We achieved similar experimental conditions to those obtained by Reid et al. The 2f spectral region used for the investigation of noise mechanisms is shown in Fig. 6-5. These traces show the 2f signal as a function of diode current taken through the 1 m multipass cell set at 32 m pathlength and at a pressure of less than 1 Torr. In Fig. 6-5.A, a small cell containing a mixture of  $\text{SO}_2$  and  $\text{N}_2$  was placed into the laser beam showing the relative position of the  $\text{SO}_2$  lines. The small

Fig. 6-5

Second harmonic scans taken through a multipass cell set for 32 m at a pressure of  $< 1$  Torr. Trace A is taken with a 10 cm cell of  $\text{SO}_2/\text{N}_2$  mixture placed in the beam. Traces B and C show high sensitivity scans taken without the 10 cm cell. Several  $\text{SO}_2$  lines are observed in trace B with a typical absorption coefficient of  $\sim 2 \times 10^{-6} \text{ m}^{-1}$ . Sensitivity is limited by optical fringes. For trace C, the phase of the lock-in amplifier was set at  $\theta + 90$  where  $\theta$  was the phase used to produce the upper traces. The phase  $\theta$  had been set to give maximum P value of the  $2f$  lineshape.



cell was removed and other scans were only taken through the multipass cell. Figure 6-5.B shows the detection of a trace of  $\text{SO}_2$  in the multipass cell. The periodicity observed in the noise clearly suggests that a part of the noise is caused by optical fringes. In the lowest trace of Fig. 6-5, the phase of the lock-in amplifier was set at  $\theta + 90$  where  $\theta$  was the phase used to produce the upper traces. The phase  $\theta$  had been set to give maximum P value of the  $2f$  lineshape. As observed in Fig. 6-5.B and 6-5.C, the  $\theta + 90$  mode operation rejects the  $\text{SO}_2$  lines and most of the systematic fringe noise present in the  $\theta$  mode. The  $\theta + 90$  mode permits one to monitor the random noise component of the noise appearing in the  $\theta$  mode.

Figure 6-6 shows three repetitive scans taken every 60 sec with a time constant of 0.3 sec. In particular, let us consider the portion of traces between 618 mA and 622 mA (i.e. between two  $\text{SO}_2$  lines). It is clear that much of the noise repeats from scan to scan. This noise is caused by optical fringes, and the pattern changes slowly as the optical pathlengths in the system fluctuate. The peak-peak amplitude of the optical fringes is equivalent to an absorption coefficient of  $\sim 7 \times 10^{-7} \text{ m}^{-1}$ . The change in fringe amplitude is equivalent to  $\sim 2 \times 10^{-7} \text{ m}^{-1}$ .

To evaluate the fluctuations of the fringes with time we fixed the laser wavelength and recorded the  $2f$  signal in


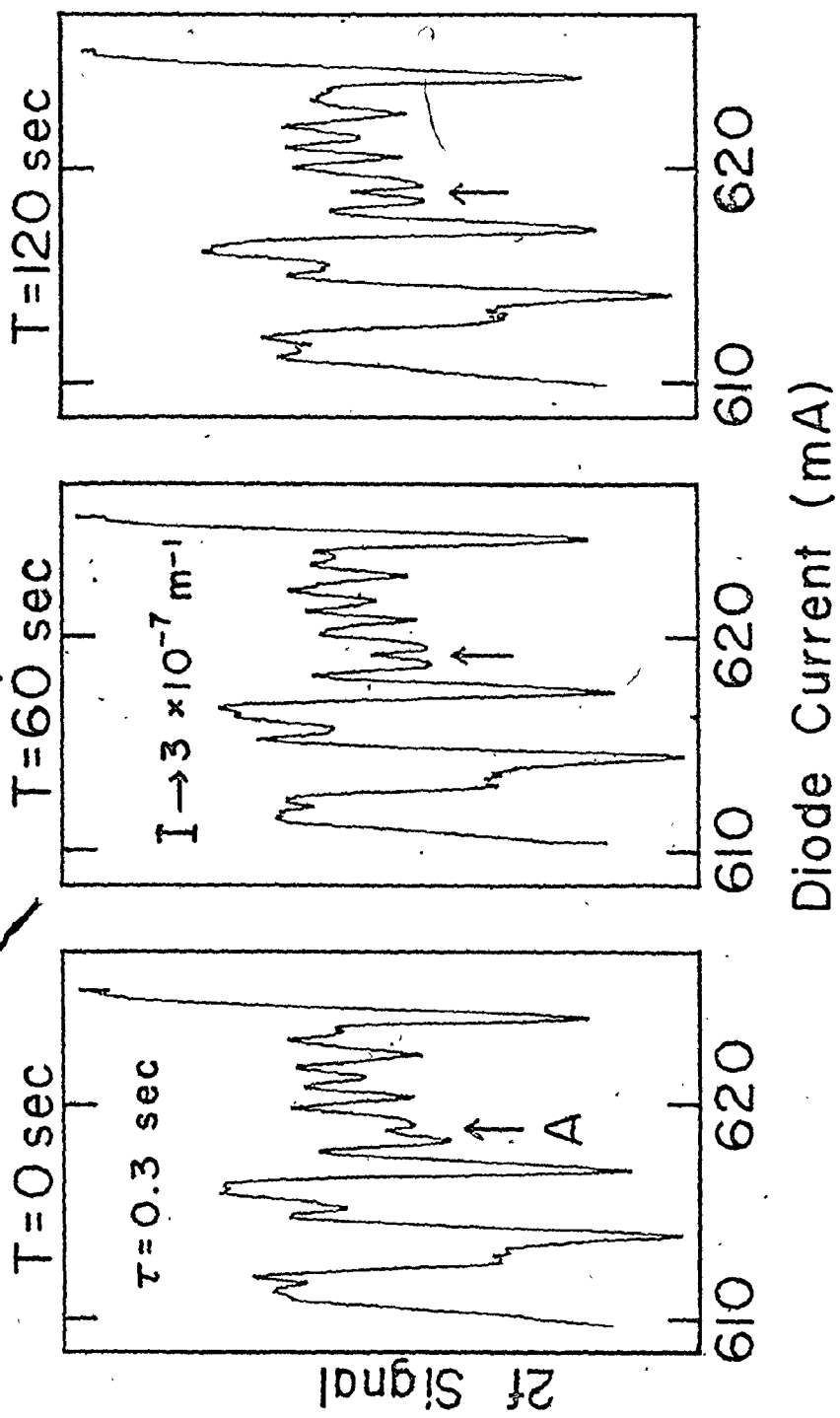


Fig. 6-6

Several diode laser scans taken every 60 sec with a time constant of 0.3 sec. The optical fringes observed between 618 mA and 622 mA changed slowly as the optical pathlengths in the system fluctuated. A typical fluctuation can be seen at the point A.



phase  $\theta$  and in quadrature  $\theta + 90$  as a function of time for several time constants. The upper traces of Fig. 6-7, taken with a time constant of 1 sec, indicate that the noise level appearing in phase limits us to detect a minimum absorption coefficient of  $\sim 2 \times 10^{-7} \text{ m}^{-1}$ . The random noise component shown in the lower trace has an amplitude  $\sim 70\%$  of the total noise level measured in phase. The measurements of  $2f$  signal as a function of time were repeated with a time constant of 10 sec. From the lower traces shown in Fig. 6-7, the minimum absorption coefficient which can be detected is  $\sim 1.3 \times 10^{-7} \text{ m}^{-1}$ . A slight decrease in the minimum absorption coefficient detected is observed by increasing the time constant from 1 sec to 10 sec. As expected, the fast fluctuations observed with a 1 sec time constant are smoothed by using a 10 sec time constant. Figure 6-8 illustrates the results obtained when the time constant is increased to 100 sec. These results clearly demonstrate that fringe noise cannot be smoothed by using longer time constant. However, the random noise is eliminated as the time constant increases. From the traces shown in Fig. 6-7 and 6-8, the contribution of systematic noise to the total noise is a minimum for a time constant of  $\sim 10$  sec and the rapid fluctuations caused by random noise are removed. In the next section, we make recommendations for increasing the sensitivity of the LAS, based on the noise characteristics shown in Fig. 6-7 and 6-8.



Fig. 6-7

Diode scans of  $2f$  signal as a function of time for a fixed diode current value. The traces were recorded simultaneously in phase  $\theta$  and in quadrature  $\theta + 90$  for a 1 sec and 10 sec time constant. Note the increase in the ratio of fringe noise to random beam noise as the time constant increases.

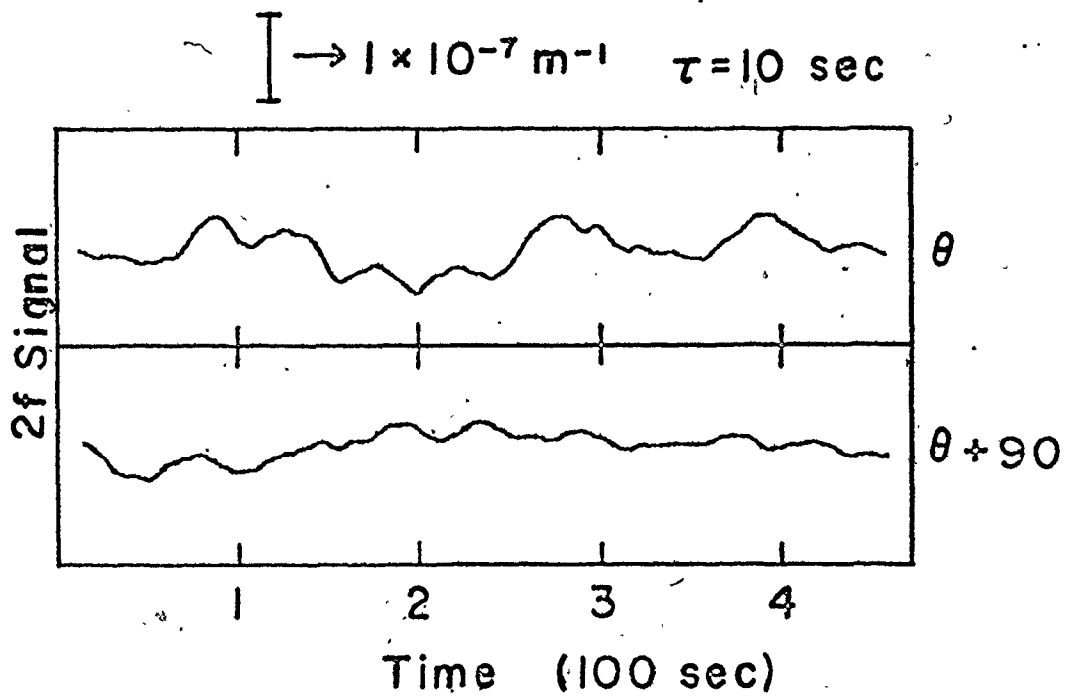
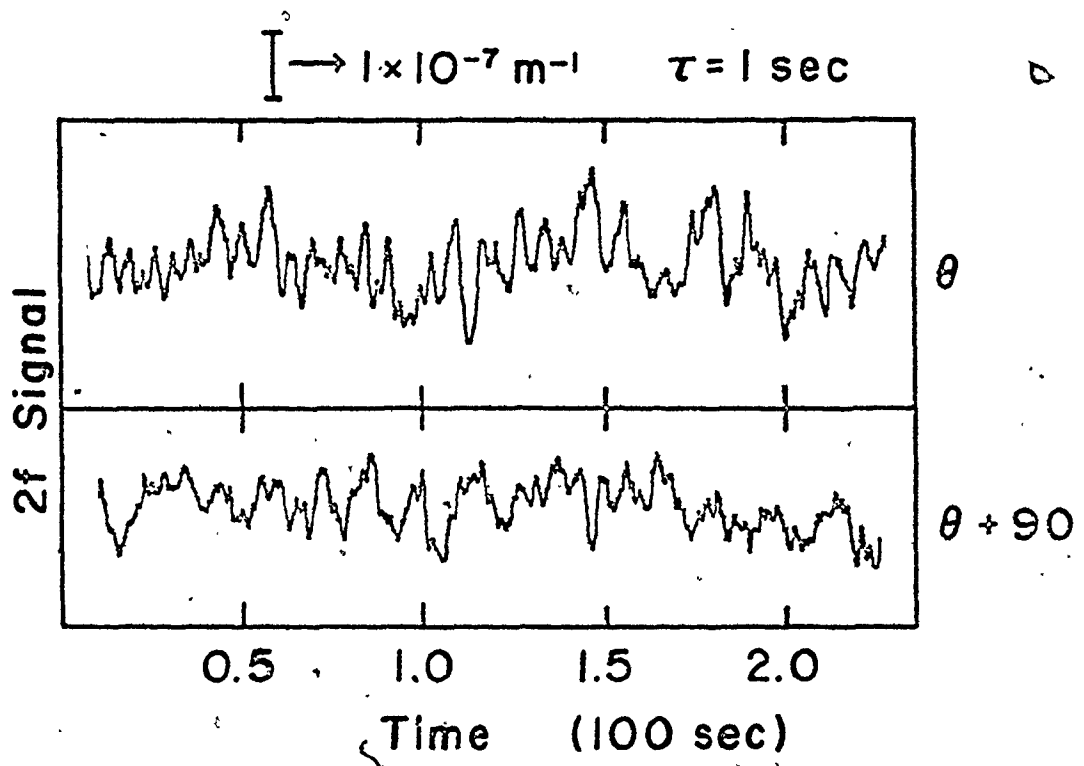
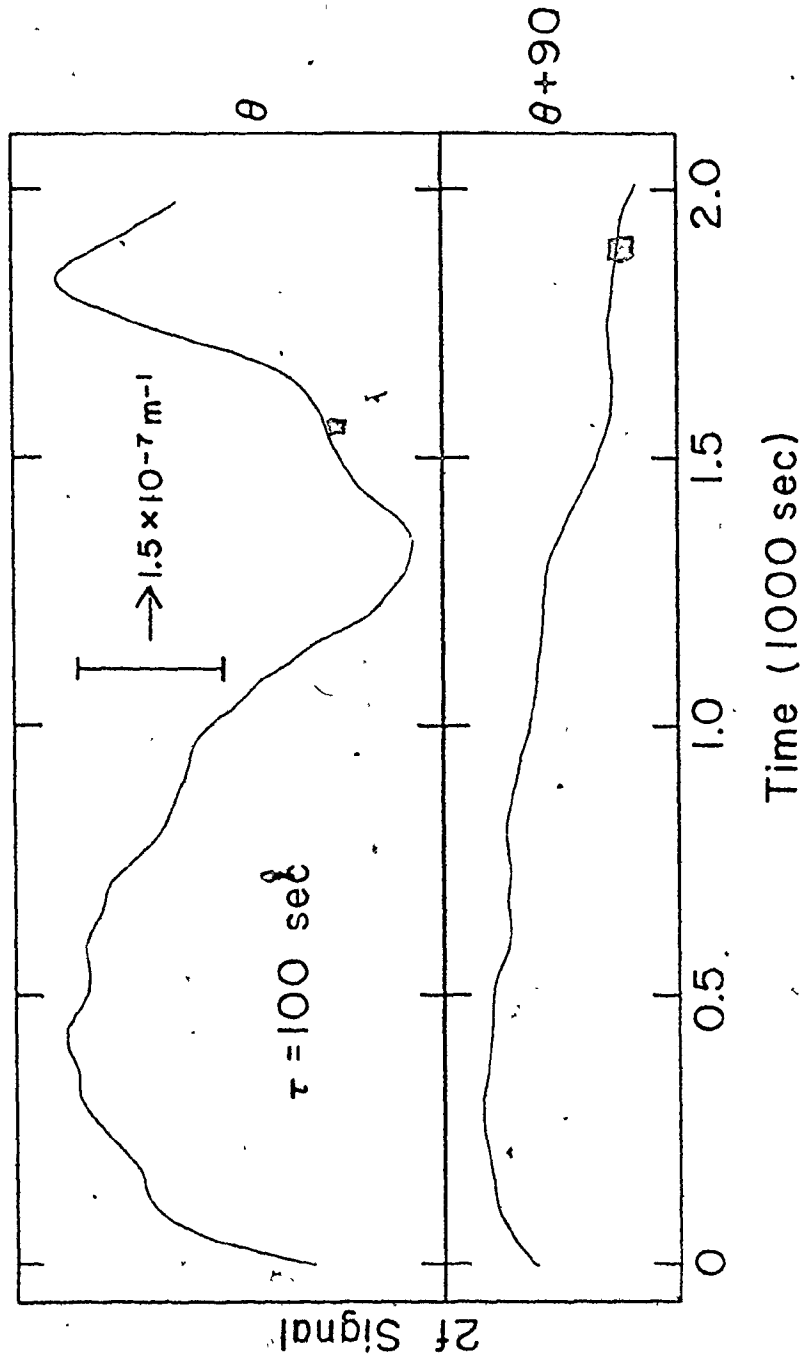


Fig. 6-8

Repeat of Fig. 6-7, but with a time constant of 100 sec.



#### 6.4 Conclusions

The noise mechanisms limiting the sensitivity of the LAS have been investigated. In our present apparatus, based on a 1 m multipass cell, optical fringe noise limits us to a sensitivity of  $\geq 1 \times 10^{-7} \text{ m}^{-1}$ . However, the simple use of a lock-in amplifier time constant as a means of signal averaging is not very effective, given the systematic nature of the optical fringe noise. We therefore recommend that the following steps be taken to increase the LAS sensitivity.

- (a) Careful attention should be paid to redesigning the optical system to reduce the magnitude of optical fringes.
- (b) A more stable optical system should be used to ensure that any remaining optical fringes are stable for periods of 30 mins, or longer.
- (c) A signal averager, with subtraction capability, can then be used to subtract the optical fringes from the  $\text{C}^{14}\text{O}_2$  signal. Even in our present system, such a signal averaging process would produce a substantial increase in sensitivity. The ultimate limitation in this technique may be the requirement that the  $\text{CO}_2$  sample must be cycled in and out of the multipass cell.
- (d) A longer cell will give a direct increase in sensitivity, but will also increase the size of the carbon sample required.

Although the improvements resulting from recommendations (a)-(d) can only be determined experimentally, we will now assume that the systematic fringe noise can be reduced to the same level as the random noise present in the system. Table 6-1 shows the LAS sensitivity and the mass of carbon required for  $C^{14}O_2$  detection at a temperature of 195 K and at a pressure of 14 Torr. The results displayed are for the P(20)  $C^{14}O_2$  line. The extrapolation of the 1 m cell results to a 10 m cell is conservative because the problems caused by the optical fringes are much less severe in a long cell [26]. Furthermore, the extrapolation of the averaging time from a time constant of 1 sec to a time constant of 10 hrs is made by assuming that the random noise decreases as the square root of the time constant. From the above considerations, radio-carbon dating by infrared absorption appears feasible.

Table 6-1

LAS sensitivity to  $C^{14}O_2$  at 195 K and 14 Torr

Multipass Cell Dimensions (m)	Mass of C gms	Sensitivity S (a)		$C^{14}$ Decay Rate (c) for S=1
		TC=1s	TC=10 hrs (b)	
L=1, $\phi = 0.1$	0.11	8	0.04	$0.028 s^{-1}$
L=10, $\phi = 0.2$	4.3	0.8	0.004	$1.1 s^{-1}$

(a) Sensitivity measured in units of  $C^{14}O_2$  concentration in a modern sample, i.e., S=1 for  $C^{14}/C^{12} = 1.3 \times 10^{-12}$ . Results are calculated assuming the P(20)  $C^{14}O_2$  line is used for detection. If the stronger P(14) line is used, all values of S are reduced by 20%.

(b) Sensitivity extrapolated from experimental results at TC=1s, assuming S/N improves as  $\sqrt{(\text{time})}$  (see text).

(c)  $C^{14}$  Radioactive decay rate in a modern sample of carbon of mass 0.11 and 4.3 gms, respectively.

CHAPTER 7  
CONCLUSIONS

The aim of this study was to investigate the feasibility of radiocarbon dating by infrared laser spectroscopy. A tunable diode laser and an optical multipass cell were used to measure the infrared absorption associated with  $C^{14}O_2$  molecules. In the first part of the research, a model representing the transfer function of the detection system was successfully developed to select the optimum experimental conditions.

It was shown that the detection of  $C^{14}O_2$  is not limited by the strong interfering lines of the stable isotopes, provided the gas sample is cooled to dry ice temperature. If one considers measurement times of a few seconds, the sensitivity limits achieved with the laser absorption spectrometer are comparable to those obtainable with an ideal  $C^{14}$  disintegration counter. An extrapolation of the LAS results to longer time constant indicates that radiocarbon dating by infrared techniques is feasible. The work reported in this thesis demonstrates that no fundamental problem should prevent the use of infrared absorption techniques for radiocarbon dating. The same techniques of infrared laser spectroscopy can also be used for the measurement of small abundances of other stable



and radioactive isotopes.

While the results described in this thesis are very promising, one is clearly not yet in a position to build a radiocarbon dating facility based on diode laser spectroscopy. Before such a project is undertaken, the present work should be extended as follows:

- (a) The optical effects causing optical fringes should be carefully investigated and eliminated, if possible. This will allow the LAS to operate at the fundamental sensitivity limit given by random laser and detector for noise.
- (b) A signal averaging/subtraction capability should be added to the present apparatus, and a systematic study made of the variation of noise levels with averaging time.
- (c) A long, cooled multipass cell should be constructed, and preliminary dating measurements carried out using samples with masses of less than 1 gm. Hopefully, these measurements can be carried out in the near future, and will confirm that radiocarbon dating by infrared absorption is a practical alternative to present techniques.

## REFERENCES

1. N.J. Van Der Merwe, "The Carbon-14 dating of iron", The University of Chicago Press, Chicago and London, 1969.
2. R.A. Muller, Physics Today, February 1979, p. 23-30.
3. J. Reid, J. Shewchun, B.K. Garside and E.A. Ballik, Opt. Eng., 17, 56-62 (1978).
4. A good bibliography on the calculations for several different lineshapes is given by M. Linger and R.L. Brown, J. of Magn. Res., 7, 335-358 (1972).
5. R. Arndt, J. Appl. Phys., 36, 2522-2524 (1965).
6. R. Le Naour, A. Le Floch and G. Stephan, Opt. and Quantum Electr., 10, 119-129 (1978).
7. G.V.H. Wilson, J. Appl. Phys., 34, 3276-3285 (1963).
8. R.A. McClatchey, W.S. Benedict, S.A. Clough, D.E. Burch, R.F. Calfee, K. Fox, L.S. Rothman, and J.S. Gareng, "AFCRL Atmospheric Absorption Line Parameters Compilation", Air Force Cambridge Research Laboratories, U.S. Air Force, AFCRL-TR-73-00096 (26 January 1973), unpublished.
9. S.S. Penner, "Quantitative molecular spectroscopy and gas emissivities", Addison-Wesley Publishing Company, Inc., U.S.A., 1959.
10. A.S. Pine and G. Guelachvili, J. Mol. Spectrosc., 79, 84-89 (1980).

11. G. Guelachvili, J. Mol. Spectrosc., 79, 72-83 (1980).
12. A. Baldacci, L. Linden, V. M. Devi, K.N. Rao and B. Fridovich, J. Mol. Spectrosc., 72, 135-142 (1978).
13. A. Baldacci, V.M. Devi, D.W. Chen, K.N. Rao and B. Fridovich, J. Mol. Spectrosc., 70, 143-159 and 160-162 (1978).
14. D. Bailly, R. Farrenq, and C. Rossetti, J. Mol. Spectrosc., 70, 124-133 (1978).
15. D.A. Steiner, T.R. Todd, C.M. Clayton, T.K. McCubbin Jr., and S.R. Polo, J. Mol. Spectrosc., 64, 438-451 (1977).
16. T.K. McCubbin Jr., J. Pliva, R. Pulfrey, W. Telfair, and T. Todd, J. Mol. Spectrosc., 136-156 (1974).
17. L.S. Rothman and W.S. Benedict, Appl. Opt., 17, 2605-2611 (1978).
18. L.S. Rothman, Appl. Opt., 17, 3517-3518 (1978).
19. C.V. Berney and D.F. Eggers Jr., J. of Chem. Phys., 40, 990-1000 (1964).
20. R.S. Eng, K.W. Nill, and M. Wahlen, Appl. Opt., 16, 3072-3074 (1977).
21. M. Wahlen, R.S. Eng, and K.W. Nill, Appl. Opt., 16, 2350-2352 (1977).
22. A. Valentin, M. Le Moal, P. Cardinet, and J. Boissy, J. Mol. Spectrosc., 59, 96-102 (1976).
23. C. Amiot and G. Guelachvili, J. Mol. Spectrosc., 59, 171-190 (1976).

24. C. Amiot, J. Mol. Spectrosc., 59, 191-208 (1976).
25. Laser Analytics, Inc. Model LO-3 Long Path Cell.
26. J. Reid, M. El-Sherbiny, B.K. Garside and E.A. Ballik, Appl. Opt., 19, October (1980).
27. W. Berger, K. Siemsen, and J. Reid, Rev. Sci. Instrum., 48, 114-116 (1977).
28. The hot CO<sub>2</sub> cell has a non-uniform temperature distribution [27]. The cell is warm in the middle, but cool at the ends. Nevertheless, the results shown in Fig. 5-2, indicate the uniform temperature model is a reasonable approximation.
29. M.J. Aitken: Physics Reports, 40, 278-351 (1978).
30. J. Reid, B.K. Garside, and J. Shewchun, Opt. and Quantum Electr., 11, 385-391 (1979).
31. J. Reid, B.K. Garside, J. Shewchun, M. El-Sherbiny, and E.A. Ballik, Appl. Opt., 17, 1806-1810 (1978).
32. R.S. Eng, A.W. Mantz, and T.R. Todd, Appl. Opt., 18, 1088-1091 (1979).